Stony Brook University

Thermal Properties of Solids: Theory and Geoscience Applications

A Dissertation Presented

by

Tao Sun

to

The Graduate School

in Partial Fulfillment of the Requirements

for the Degree of

Doctor of Philosophy

in

Physics

Stony Brook University

August 2008

Stony Brook University

The Graduate School

Tao Sun

We, the dissertation committee for the above candidate for the Doctor of Philosophy degree, hereby recommend acceptance of this dissertation.

Philip B. Allen – Dissertation Advisor
Professor, Department of Physics and Astronomy

Harold J. Metcalf – Chairperson of Defense
Professor, Department of Physics and Astronomy

María V. Fernández-Serra
Assistant Professor, Department of Physics and Astronomy

Renata M. M. Wentzcovitch
Professor, Department of Chemical Engineering and Materials Science
University of Minnesota

This dissertation is accepted by the Graduate School.

Lawrence Martin
Dean of the Graduate School

Abstract of the Dissertation

Thermal Properties of Solids: Theory and Geoscience Applications

by

Tao Sun

Doctor of Philosophy

in

Physics

Stony Brook University

2008

This thesis reports on the theoretical studies of the thermal properties of platinum and ferropericlase. Both materials are important for geoscience. Platinum is a widely used high pressure standard. However the established thermal equation of state has uncertainties, especially in the high P-T range. We use density functional theory to calculate the thermal equation of state of platinum, up to 550 GPa and 5000 K. The static lattice energy is computed by using the LAPW method, with LDA, PBE, and the recently proposed WC functional. The electronic thermal free energy is evaluated using the Mermin functional. The vibrational part is computed within the quasi-harmonic approximation using density functional

perturbation theory and pseudopotentials. Special attention is paid to the influence of the electronic temperature to the phonon frequencies. We find that in overall LDA results agree best with the experiments. Based on the DFT calculations and the established experimental data, we develop a consistent thermal EOS of platinum as a reference for pressure calibration. Ferropericlase, ($Mg_{1-x}Fe_xO$, with $x = 0.10 - 0.15$), is thought to be one of the major constituents of the earth's lower mantle ($660 - 2900$ km depth). We measured the temperature dependence of the reflectance spectra of magnesium oxide (MgO) and ferropericlase ($Mg_{1-x}Fe_xO$, for $x = 0.06$ and $x = 0.27$) over a wide frequency range (≈ 50 to $32\,000$ cm^{-1}) at 295 and 6 K. The complex dielectric function has been determined from a Kramers-Kronig analysis of the reflectance. The spectra of the doped materials resemble pure MgO in the infrared region, but with much broader resonances. We use a shell model to calculate the dielectric function of ferropericlase, including both anharmonic phonon-phonon interactions and disorder scattering.

Contents

List of Figures

List of Tables

Preface

This thesis consists of two parts. The first part is on the thermal equation of state of platinum. This work was carried out during my stay in Minneapolis, under the supervision of Prof. Renata M. Wentzcovitch. It is published in Phys. Rev. B 78, 024304 (2008). The second part is on the infrared properties of ferropericlase. This work was finished under the supervision of Prof. Philip B. Allen. It is published in Phys. Rev. B 77, 134303 (2008)

Chapter 1 provides the backgrounds of studying the thermal equation of state (EOS). I give a brief introduction on the significance of the thermal EOS, and the experimental methods to determine it. Then I review the basics of the electronic structure theory. Chapter 2 is a reproduction of the paper on platinum EOS as appeared in Phys. Rev. B. My coauthors are K. Umemoto, Z. Q. Wu, J. C. Zheng and R. M. Wentzcovitch. Dr. Umemoto taught me how to generate pseudopotentials. Dr. Wu helped me in calculating the thermal properties. Dr. Zheng did the zero-temperature static linearized augmented plane-wave (LAPW) calculation. I did the pseudopotential calculations on static, vibrational and electronic thermal energies. The data analysis and the write-up of the paper were done by me. Chapter 3 summarized the empirical shell lodel and linear response theory. They serve as supporting materials for chapter 4. Chapter 4 is a reproduction of the manuscript

Chapter 1

Preliminaries on Equation of State

1.1 Equation of State

The Equation of State (EOS) of materials is fundamentally important, for both theoretical and practical reasons. The EOS reflects a material's composition, and its internal interactions. To predict the EOS with better accuracy is one major impetus driving the development of the electronic structure theory. On the more practical side, determining the thermal EOS of minerals is the main task of high pressure mineral physics.[6] By measuring the thermal EOS of minerals in laboratory with tools like the laser-heated diamond anvil cell (DAC), geophysicists determine the density, bulk modulus and speed of the elastic waves of minerals at high pressures and high temperatures. Comparing the speed of the elastic waves with those from seismological observations, they further infer the composition, pressure and temperature profile of the earth's interior.

The EOS of the ideal gas, $PV = nRT$, is the most famous EOS in physics. For solids the effect of temperature is much less prominent than for gas. People mostly

start with isothermal EOS, $P(V)$ at constant T. The temperature effect is accounted for by thermal pressure, which is defined as

$$P_{\text{th}} = P(V,T) - P(V,T_0) = \int_{T_0}^{T} \alpha K_T dT. \tag{1.1}$$

where T_0 is the reference temperature. α is the thermal expansivity, K_T is the bulk modulus at constant temperature.

$$\alpha(P,T) = -\frac{1}{V}\frac{\partial V}{\partial T}\Big|_{P}$$
$$K_T(V,T) = V\frac{\partial P}{\partial V}\Big|_{T} \tag{1.2}$$

Equation (1.1) can be easily proven from relation among partial derivatives.

$$\frac{\partial V}{\partial T}\Big|_{P}\frac{\partial P}{\partial V}\Big|_{T}\frac{\partial T}{\partial P}\Big|_{V} = -1 \tag{1.3}$$

Once the isothermal EOS $P(V,T_0)$ at T_0 (usually at room temperature), the thermal expansivity α and bulk modulus K_T are known, the thermal EOS of the material is determined. A great simplification is the product αK_T depends on temperature and volume weakly for many materials. That is, the thermal pressure P_{th} is linear in temperature and independent of volume, within good approximation. This fact is very useful in practice.

The isothermal EOS of a material is determined experimentally by putting the sample, together with some reference material which has simple crystal structure and established isothermal EOS (pressure scale), into a high pressure apparatus. The most widely used high pressure apparatus is the DAC. The volumes of the sample

2
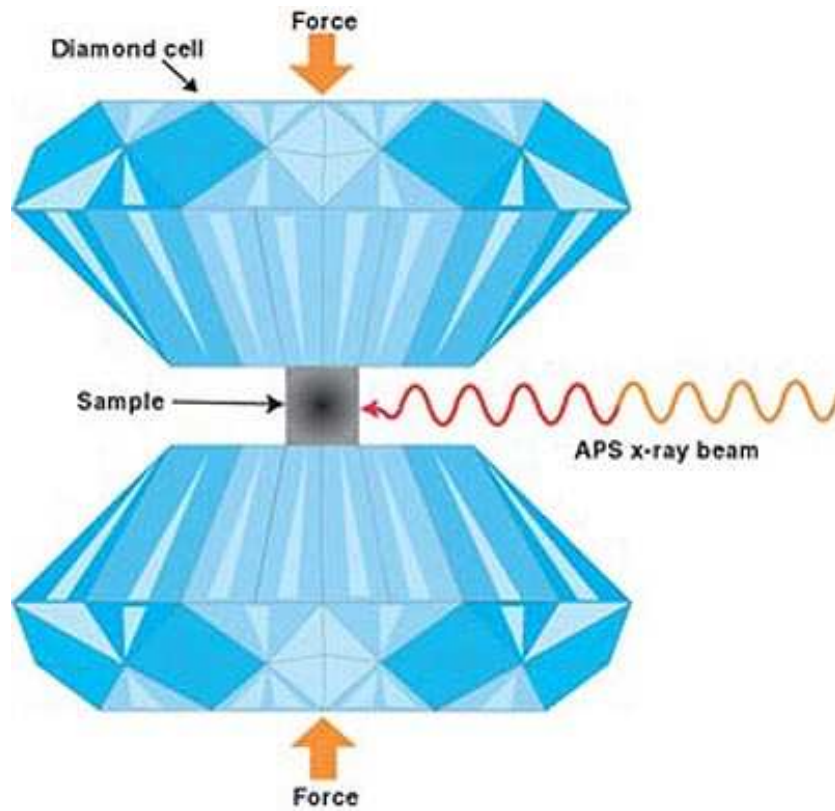
Figure 1.1: Illustration of a diamond anvil cell (from www.aps.anl.gov)

and the reference are determined by X-ray diffraction. From the isothermal EOS of
the reference one reads pressure at measured volume. Since the sample and reference
are submerged in a hydrostatic or quasi-hydrostatic medium (He, Ar, KBr), their
pressure are assumed to be the same. An illustration of the DAC is shown in Fig. 1.1

The feasibility and accuracy of pressure measurements in DAC experiments de-
pends critically on the reliability of the EOS of the reference material. The thermal
EOS of the reference must be established first to be used as a pressure scale. Shock
wave compression provides a way to find P-V-T relations of a material without re-
lying on other references. Shock wave compresses a sample so fast that there's little
thermal exchange to the environment. That is, it is an adiabatic process. The change

in kinetic and internal energy (temperature) is caused by the volume work done by the shock wave. This results in the famous Rankine-Hugoniot equation

$$E_H(V,T) - E_i(V_0, T_i) = (P_H(V,T) + P_0(V_0, T_i))\frac{V_0 - V}{2}, \qquad (1.4)$$

where $E_H(V,T)$ and $P_H(V,T)$ are the internal energy, pressure at volume V and temperature T. $E_i(V_0, T_i)$ and $P_0(V_0, T_i)$ are the internal energy, pressure at the initial volume V_0 and temperature T_i. During a shock wave experiment, the movement of the shock wave is monitored by fast photographs. From these photos the velocities of the shock wave and the sample particles are calculated, the pressure P_H is derived from momentum conservation. Then, with some assumptions of the internal energy, the room temperature isotherm can be obtained from the Rankine-Hugoniot equation.

Experiments can only measure P-V-T at discrete points. Some analytical formula is necessary to interpolate pressure at any particular volume. The most widely used formula is the Birch-Murnahan equation[7](BM)

$$
\begin{aligned}
P(V,T) &= \frac{3}{2}K_0(T)[(V/V_0(T))^{-\frac{7}{3}} - (V/V_0(T))^{-\frac{5}{3}}] \cdot \{1 \\
&+ \frac{3}{4}(K_0'(T) - 4)[(V/V_0(T))^{-\frac{2}{3}} - 1] + \frac{3}{8}[K_0(T)K_0''(T) \\
&+ (K_0'(T) - 3)(K_0'(T) - 4) + \frac{35}{9}][(V/V_0(T))^{-\frac{2}{3}} - 1]^2\} \qquad (1.5)
\end{aligned}
$$

and the Vinet equation.[8]

$$P(V,T) = 3K_0(T)\,(V/V_0(T))^{-\frac{2}{3}}\,(1 - (V/V_0(T))^{\frac{1}{3}})e^{\frac{3}{2}(K_0'(T)-1)(1-(V/V_0)^{\frac{1}{3}})} \quad (1.6)$$

where $V_0(T)$ is the equilibrium volume at temperature T. $K_0(T)$, $K_0'(T)$ and $K_0''(T)$ are bulk modulus, derivative of the bulk modulus and second derivative of the bulk modulus at volume V_0 at temperature T, respectively.

1.2   Density Functional Theory (DFT)

Electronic structure theory, which is the basis for understanding the physical properties of the materials, requires a solution of the electronic Schrödinger equation[9, 10]

$$\hat{h}_e \Phi(\mathbf{R}, \mathbf{r}) = \epsilon(\mathbf{R}) \Phi(\mathbf{R}, \mathbf{r}) \tag{1.7}$$

for a system of N interacting electrons in the external Coulomb potential generated by a collection of atomic nuclei. The many-electron wave function $\Phi(\mathbf{R}, \mathbf{r})$ has the nuclear coordinates $\mathbf{R}$ as parameters. The eigenvalues $\epsilon(\mathbf{R})$ also depend parametrically on $\mathbf{R}$, and define the adiabatic potential energy surfaces. The electronic Hamiltonian

$$\hat{h}_e = -\sum_{i=1}^{N} \frac{\hbar^2}{2m} \nabla_i^2 + \frac{e^2}{2} \sum_{i=1}^{N} \sum_{j \neq i} \frac{1}{|\mathbf{r}_i - \mathbf{r}_j|} - e^2 \sum_{I=1}^{P} \sum_{i=1}^{N} \frac{Z_I}{|\mathbf{R}_I - \mathbf{r}_i|} \tag{1.8}$$

contains two-body electron-electron interactions. This makes it difficult to solve the problem exactly. The basic idea of DFT is to replace the two-body interactions by a one particle mean field potential, and solve an equivalent one particle problem. The general validity of the approach is guaranteed in principle by the Hohenberg-Kohn theorem.[11] However, the exact form of the one particle mean field potential is unknown, and people resort to all kinds of approximations. The most widely used ones are the local density approximation (LDA)[12], and the generalized gradient

approximation (GGA)[13].

1.3   Pseudopotentials

DFT has several different implementations, with different accuracy and computational speed. Each is suitable for a certain kind of problems. Plane wave pseudopotential implementation is probably the most efficient of all. It is based on the observation most of the properties of the materials are determined by a few valence electrons of the constituent atoms. The core electrons, being tightly bonded near the nuclei, require much higher energy to get excited. The effects of the core electrons on the valence electrons can be described by pseudopotentials. Using pseudopotentials allows us to eliminate core electrons, and save considerable computation time. The quantitative way to describe how well pseudopotentials can mimic the real potentials is to compare their scattering properties: The logarithmic derivatives of the real and pseudo wave function and their first energy derivatives should agree. This property is crucial for the pseudopotential to have optimum transferability among a variety of chemical environments.[14, 15] For norm-conserved pseudopotentials, the conditions for conserving charge and transferability are equivalent.

Figure 1.2 shows the log derivatives of the Vanderbilt ultrasoft pseudopotential[16] (denoted as pseudo-1 in the paper) that we use to compute the vibrational properties of platinum.

The other criterion to judge the accuracy of the pseudopotential is to compare the electronic band structure computed by using the all-electron full-potential method. Fig. 1.3 shows the electronic structure of platinum computed by LAPW and pseudo-1. Besides the good agreement, no 'ghost state'[17] appears in the bandstructure.
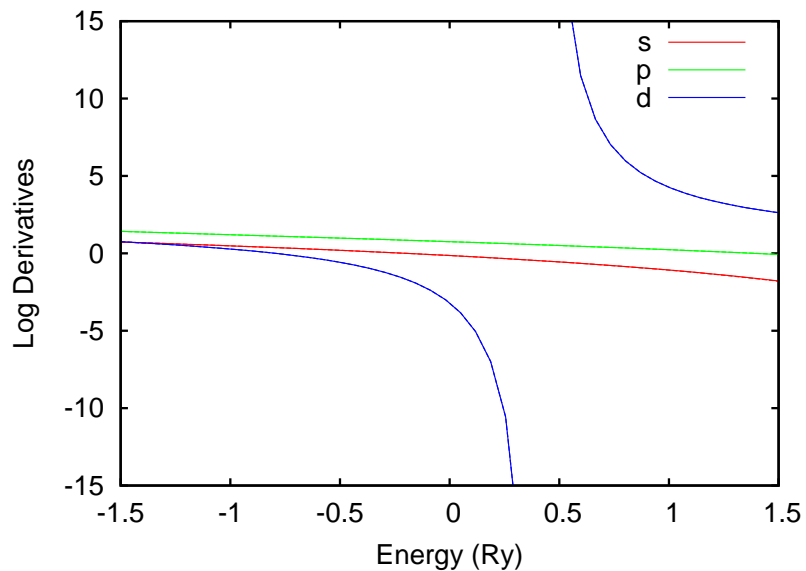
Figure 1.2: Energy dependence of logarithmic derivatives at $r = 2.2$ a.u. for Pt full-core atomic wave functions (solid lines) and pseudo wave functions (broken lines). The agreements are so good that they are indistinguishable on the current scale.
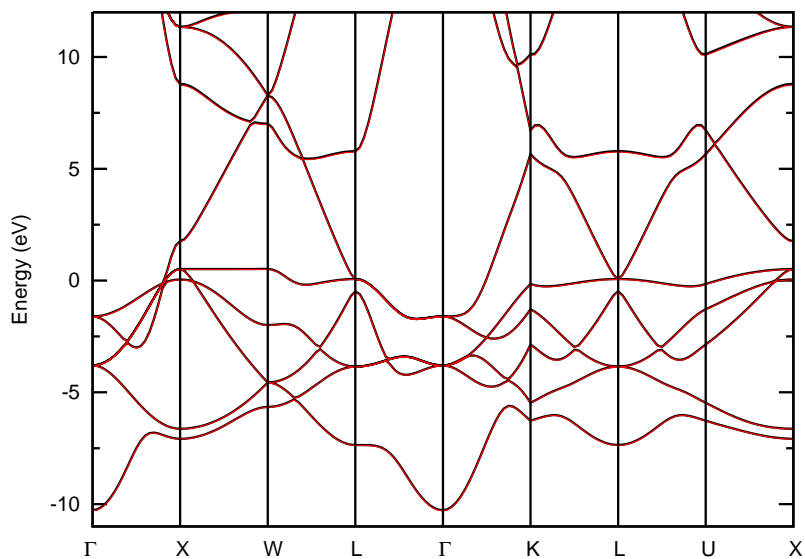
Figure 1.3: Electronic band structure of platinum computed by using pseudopotential(Red) and LAPW method(Black) at the experimental ambient volume.

Chapter 2

Lattice Dynamics and Thermal Equation of State of Platinum

2.1 Introduction

Platinum (Pt) is a widely used high-pressure standard. Its equation of state (EOS) at room temperature has been established by reducing shock Hugoniot [1, 5, 18, 19] and by *ab initio* linear-muffin-tin-orbital (LMTO) calculations[1] up to 660 GPa. Mao *et al.*[20] used the EOS developed in Ref. [1] (Holmes *et al.*) to calibrate pressure in their compression experiment on Fe and Fe-Ni alloy. The bulk moduli measured at the earth's core pressure are substantially higher than those extrapolated from seismological observations.[21, 22] A large pressure offset is needed to remove the discrepancy: about 8% at 100 GPa, 15% at 300 GPa. The origin of this offset is under investigation. One possibility is the EOS of Holmes *et al.* seriously overestimates pressure.[21] Singh raised other possibilities.[22] He noticed that the one-parameter EOS of platinum agrees with the EOS of Holmes *et al.* to 1 % at high pressures, and

concluded that large systematic error in pressure scale is unlikely. He further proposed that the discrepancy is due to the pressure on the sample is different from the one on the pressure standard, in the high-pressure X-ray diffraction measurements.

There are conflicting reports on the uncertainties of Holmes *et al.*'s EOS. Dewaele *et al.*[3] measured the EOS of six metals at ambient temperature to 94 GPa using a diamond anvil cell (DAC). By cross-checking different pressure scales they found Holmes *et al.*'s EOS overestimates pressure by ≈ 4 GPa near 100 GPa at room temperature. This conclusion is confirmed by other groups.[23, 24] While more recent calculations based on density functional theory (DFT) suggest Holmes *et al.*'s EOS underestimates, rather than overestimates, pressure. Xiang *et al.*[25] computed the thermal equation of state of platinum using LMTO and a mean field potential method. The pressure they obtained is 5 to 6 % higher than that of Holmes *et al.* at high pressures. Menéndez-Proupin *et al.* [2] reached similar conclusion using pseudopotentials. Both calculations employ the local density approximation (LDA) functional.[12] And the excess pressure is attributed to LDA in Ref. [2]. However it can also be caused by other factors. In Table II of Ref. [25], the equilibrium volume decreases as the temperature increases. The electronic thermal pressure is negative according to this calculation, which is contrary to expectations. Ref. [2] uses an ultrasoft Rappe-Rabe-Kaxiras-Joannopoulos pseudopotential from the PWSCF website,[26] which contains only $5d$, $6s$ and $6p$ valence states. Its large cutoff radius (2.6 a.u.) may cause error in studying the highly compressed structure.

Besides the room temperature isotherm, accurate thermal pressure (P_{th}) is needed to calibrate pressure in simultaneous high-pressure and high-temperature experiments. Experiments cannot easily determine P_{th} over a wide temperature and volume range.[27] Consequently P_{th} is often estimated by assuming it is linear in temperature

9

and independent of volume.[1, 5] Theory can in principle do better. In quasi-harmonic approximation (QHA), DFT calculations give P_{th} at any particular temperature and volume. It is desirable to combine the experimental data with DFT calculations, taking the advantages of both, and construct a more accurate thermal EOS for pressure calibration.

In this paper we have three goals: first is to check the accuracy of the theoretical EOS of platinum predicted by different exchange correlation functionals. In contrast with previous calculations, we find the room temperature isotherm computed with LDA lies below, and nearly parallel to the experimental compression data. The Fermi level of platinum lies in the d band and gives a very large density of state (DOS) $N(E_{\text{F}})$. Its vibrational frequencies are more sensitive to the electronic temperature than those of many other metals. A Kohn anomaly has been observed in platinum at 90 K.[28] It becomes weaker and finally disappears when the temperature increases. Thus our second goal is to discuss the electronic temperature dependence of vibrations (ETDV) and its influence on the thermal properties. Our last goal is to provide an accurate thermal EOS for pressure calibration. For this purpose we make corrections to the raw DFT results. We correct the room temperature Gibbs free energy $G(P, 300 \text{ K})$ to ensure that it reproduces the experimental isotherm, then combine it with the DFT calculated temperature dependence to get $G(P, T)$. The thermal EOS and thermal properties deduced from the corrected Gibbs free energy are in good agreement with the known experimental data.

2.2 Computational Method

The EOS of a material is determined by its Helmholtz free energy $F(V,T)$, which consists of three parts:

$$F(V,T) = U(V) + F_{\mathrm{vib}}(V,T) + F_{\mathrm{ele}}(V,T), \tag{2.1}$$

where $U(V)$ is the static energy of the lattice, $F_{\mathrm{vib}}(V,T)$ is the vibrational free energy, $F_{\mathrm{ele}}(V,T)$ accounts for the thermal excitation of the electrons. $U(V)$ is calculated by using the linearized augmented plane-wave (LAPW) method[29] and three different exchange-correlation functionals: LDA, Perdew-Burke-Ernzerhof (PBE),[30] and Wu-Cohen (WC).[31] The $4f$, $5s$, $5p$, $5d$, $6s$ are described as valence states, others are treated as core states. The convergence parameter RK_{max} is 10.0, and the muffin-tin radius R is 2.08 a.u.. A $16 \times 16 \times 16$ Monkhorst-Pack[32] uniform k-grid is used and the integration over the whole Brillouin zone is done with the tetrahedron method.[33] All the calculations using LAPW are performed with and without spin-orbit effect.

In contrast with the static lattice energy $U(V)$, which is sensitive to the relaxation of the core states and requires a full-potential treatment, thermal excitations contribute to much smaller energy variations and mostly depend on the valence states. We use pseudopotentials to compute the thermal effects. An ultra-soft Vanderbilt pseudopotential[16] is generated from the reference atomic configuration $5s^2 5p^6 5d^9 6s^1 6p^0$, including non-linear core corrections.[34] There are two projectors in the s channel, $5s$ and $6s$; two in the p channel, $5p$ and an unbound p at 0.2 Ry above the vacuum level; one in the d channel, $5d$. The local component is set in the f channel at the vacuum level. The cutoff radii for each channel s, p, d and local

are 1.8, 1.9, 1.9 and 1.8 a.u., respectively. We use the scalar relativistic approximation and spin-orbit effect is not included. This pseudopotential reproduces the LAPW electronic band structure, both at the most contracted volume and the 0 GPa experimental volume. We find pseudopotentials with different exchange-correlation functionals yield very similar electronic band structures for platinum, and we use LDA to compute all the thermal effects.

We consider 20 different volumes, with lattice constants from 7.8 to 6.2 a.u.(17.58 Å^3 to 8.83 Å^3 in volume). For each volume V_i, we use LAPW to compute its static energy $U(V_i)$ and the LDA pseudopotential to evaluate its thermal free energy $F_{\text{vib}}(V_i, T)$ and $F_{\text{ele}}(V_i, T)$. $F_{\text{vib}}(V_i, T)$ is treated within QHA with phonon frequencies dependent on electronic temperature (denoted as eQHA) as

$$F_{\text{vib}}^{\text{eQHA}}(V_i, T) = \frac{1}{2} \sum_{\mathbf{q},j} \hbar\omega_{\mathbf{q},j}(V_i, T_{\text{ele}}) + k_{\text{B}}T \sum_{\mathbf{q},j} \ln(1 - \exp(\frac{-\hbar\omega_{\mathbf{q},j}(V_i, T_{\text{ele}})}{k_B T})), \quad (2.2)$$

where $\omega_{\mathbf{q},j}(V_i, T_{\text{ele}})$ denotes the phonon frequency computed at volume V_i and electronic temperature T_{ele}. In thermal equilibrium the system temperature T, the ionic temperature T_{ion}, and T_{ele} are equal. We distinguish these three temperatures to emphasis the temperature dependence of phonon frequencies come from different sources. Anharmonic phonon-phonon interactions cause phonon frequencies to depend on T_{ion}, but they are omitted in QHA. Electronic thermal excitations disturb the charge distribution in the crystal and cause phonon frequencies depend on T_{ele}. In the normal QHA used for insulators and some metals, this effect is also ignored and $\omega_{\mathbf{q},j}$ has no temperature dependence (except through $V(T)$). Platinum has a larger $N(E_{\text{F}})$ than many other metals and ETDV may have noticeable effects on its thermal properties. To quantitatively measure the influence of ETDV, we compare the vibrational free

energies at volume V_i and temperature T_j (T_j=500, 1000, ... 5000 K) computed without/with ETDV. Without ETDV (normal QHA), phonon frequencies are computed at T_{ele}=0 K by using Methfessel-Paxton[35] (MP) smearing with a smearing parameter of 0.01 Ry. The corresponding vibrational free energy is denoted as $F_{\mathrm{vib}}^{\mathrm{QHA}}(V_i, T_j)$. With ETDV (eQHA) phonon frequencies have to be computed separately for each T_j. This is achieved by using the Mermin functional[36] and Fermi-Dirac (FD) smearing. The corresponding vibrational free energy is denoted as $F_{\mathrm{vib}}^{\mathrm{eQHA}}(V_i, T_j)$. The difference between these two, $\Delta F_{\mathrm{ETDV}}(V_i, T_j){=}F_{\mathrm{vib}}^{\mathrm{eQHA}}(V_i, T_j) - F_{\mathrm{vib}}^{\mathrm{QHA}}(V_i, T_j)$, describes the correction caused by ETDV. To get ΔF_{ETDV} at arbitrary temperature between 0-5000 K we fit a 4th order polynomial from $\Delta F_{\mathrm{ETDV}}(V_i, T_j)$

$$
\begin{aligned}
\Delta F_{\mathrm{ETDV}}(V_i, T) &= F_{\mathrm{vib}}^{\mathrm{eQHA}}(V_i, T) - F_{\mathrm{vib}}^{\mathrm{QHA}}(V_i, T) \\
&= a_1(V_i) \cdot T + a_2(V_i) \cdot T^2 + a_3(V_i) \cdot T^3 + a_4(V_i) \cdot T^4. \quad (2.3)
\end{aligned}
$$

The final vibrational free energy is computed as $F_{\mathrm{vib}}(V_i, T){=}F_{\mathrm{vib}}^{\mathrm{QHA}}(V_i, T){+}\Delta F_{\mathrm{ETDV}}(V_i, T)$ (we omit the subscript 'eQHA' and denote $F_{\mathrm{vib}}^{\mathrm{eQHA}}$ as F_{vib}).

Phonon frequencies in the above procedure are determined by density functional perturbation theory (DFPT)[37] as implemented in the Quantum ESPRESSO[38] package. The dynamical matrices are computed on an $8 \times 8 \times 8$ **q**-mesh (29 **q** points in the irreducible wedge of the Brillouin Zone). Force constant interpolation is used to calculate phonon frequencies at arbitrary **q** vectors. The summation in Eq. (2.2) is evaluated on a $32 \times 32 \times 32$ **q**-mesh.

The electronic free energy $F_{\mathrm{ele}}(V_i, T)$ is determined by using the Mermin functional[36] and Fermi-Dirac smearing. Similar to getting $F_{\mathrm{vib}}(V_i, T)$, we first compute F_{ele} at ev-

ery 50 K from 50 K to 5000 K, then we fit them to a 4th order polynomial

$$F_{\text{ele}}(V_i, T) = b_1(V_i) \cdot T + b_2(V_i) \cdot T^2 + b_3(V_i) \cdot T^3 + b_4(V_i) \cdot T^4. \qquad (2.4)$$

Terms other than $b_2(V_i)T^2$ represent deviations from the lowest-order Sommerfeld expansion $F_{\text{ele}} = -\frac{\pi^2}{6} N(E_{\text{F}}, V_i)(k_B T)^2$, where $N(E_{\text{F}}, V_i)$ is the electronic density of states at Fermi energy E_{F} and volume V_i. We find below 1000 K, keeping only the quadratic term does not introduce much error. The influence of the higher order terms becomes prominent at high temperatures. At 2000 K, the error reaches about 15 %. The fitted quadratic coefficient $b_2(V_i)$ differs from the Sommerfeld value $-\frac{\pi^2}{6} N(E_{\text{F}}, V_i)k_B^2$ by 5 % (V_i=8.83 Å^3) to 15 % (V_i=15.63 Å^3). It seems the Sommerfeld expansion works better at high pressures, where the electronic bands are more dispersive and $N(E_{\text{F}})$ is smaller. We combine $F_{\text{ele}}(V_i, T)$ with the static energy $U(V_i)$ from LAPW and the vibrational free energy $F_{\text{vib}}(V_i, T)$ from the same pseudopotential to get the total free energy $F(V_i, T)$ at volume V_i. There are two popular parameterized forms to fit the total free energy $F(V, T)$, 4th order Birch-Murnahan[7](BM) and Vinet.[8] We find BM and Vinet are comparable in accuracy to fit the static and low temperature free energy, but BM yields much lower residual energies than Vinet for the high temperature results. Thus we use 4th order BM to get $F(V, T)$. Other thermodynamical properties are computed by finite difference.

All the pseudopotential calculations are carried out with the same plane-wave cutoff of 40 Ry, charge-density cutoff of 480 Ry, and a shifted $16 \times 16 \times 16$ Monkhorst-Pack mesh. To determine the convergence uncertainties of our results, we choose one volume ($V_i = 15.095$ Å^3) and recompute its phonon frequencies at $T_{\text{ele}} = 0$ K, with a $24 \times 24 \times 24$ mesh and a higher plane-wave cutoff (60 Ry). The two sets of phonon

frequencies differ by 0.5 % at most. The corresponding $F_{\mathrm{vib}}^{\mathrm{QHA}}$ differ by 0.07 mRy/atom at 2000 K, 0.18 mRy/atom at 5000 K. The influence of ETDV is much greater than the convergence uncertainties. For some modes phonon frequencies change by 10 % or more from T_{ele}=500 K to T_{ele}=2000 K. The free energy correction ΔF_{ETDV} is about 1 mRy at 2000 K.

2.3 Summary of Previous Works

Besides the two calculations[2, 25] mentioned in the introduction, which focus on the thermal EOS of platinum, there are some other papers related to this subject. Cohen *et al.*[39] computed the static EOS of platinum using LAPW and PBE, and treated it as an example to discuss the accuracy of different EOS formations. They found Vinet fitted better than 3rd order BM. The accuracy of 4th order BM and Vinet were comparable. Tsuchiya *et al.*[40] computed the electronic thermal pressure (P_{ele}) of Au and Pt using LMTO and LDA. At 2200 K, P_{ele} is 1.01 GPa for Pt, while only 0.06 GPa for Au. This is caused by the different $N(E_{\mathrm{F}})$ of the two metals. The small ETDV effect (1 % change in phonon frequency from T_{ele}= 0 K to 3000 K) observed on gold[41] is consistent with this picture. Wang *et al.*[42] used LAPW and an average potential method to determine the thermal contributions. Then they reduced the experimental shock Hugoniot and got the room temperature isotherm of Pt. This isotherm is very similar to that of Holmes *et al.*, in spite of the fact that in the latter case, thermal pressure is estimated semi-empirically. Ref. [43] computed the static EOS of platinum using pseudopotentials with/without spin-orbit effects up to 150 GPa. In the following section, we compare our calculations with these previous ones whenever appropriate.

On the experimental side, The reduced isothermal P-V-T EOS from shock wave experiments are widely used as primary pressure scales. At present they are also the only experimental sources for P-V-T data at very high pressures. The shock Hugoniot of platinum was first obtained by using chemical explosives.[5] The reduced room temperature isotherm was up to 270 GPa. Holmes *et al.*[1] went to higher compression ratio using a two-stage light-gas gun. The final shock Hugoniot is a combination of these two sets of data. In spite of the crucial role of the reduced shock EOS, its accuracy suffers from low precision in measurements, and theoretical simplifications made in the reducing process.[24, 44] With the development of DAC and third-generation synchrotron light source, cross-checking different pressure scales became feasible. More accurate thermal EOS were obtained by using this method.[3, 27]

Recently, Dorogokupets *et al.*[4] constructed a semi-empirical model to describe the thermal properties of Al, Au, Cu, Pt, Ta and W, The model contains about 20 parameters, which are fitted to the available experimental data on the heat capacity, enthalpy, volume, thermal expansivity, bulk modulus and shock Hugoniot. Based on this model they reanalyzed the data in Ref. [3] up to 100 GPa. The resulting EOS, which are consistent with the measured thermal properties, are believed to be more accurate than the original in the corresponding pressure range.[45] A simplified version of the model[46] yields similar EOS at low pressures. However their high pressure extrapolations differ by 2.5 % near 240 GPa. It will be interesting to use DFT to explore the EOS at very high pressures, which are still out of reach for the current DAC experiments.

2.4　Results and Discussions

2.4.1　Static Equation of State

Before studying the EOS at finite temperature, we examine the static EOS computed by using different exchange-correlation functionals, and compare them with previous calculations. Excluding the thermal effects (which amount to ≈ 2 GPa at room temperature) helps to identify the origin of their differences. Fig. 2.1 shows the static pressure vs. volume relations using different exchange-correlation functionals. The corresponding EOS parameters are listed in Table 2.4.1. The experimental data at room temperature are also included in the figure to give a rough estimate of the difference. Comparing to the experiments, in the entire volume range LDA underestimates pressure while PBE overestimates. WC improves on PBE, but still overestimates. A detailed comparison between the calculated room temperature isotherms (including the thermal effects) and the experimental data will be given in Sec. 2.4.3. DFT has many different implementations, such as LAPW, LMTO, and various pseudopotentials. If the calculations are good, they should yield similar results. We compare our LDA calculations with previous ones in Fig. 2.2. Two of our own pseudopotential calculations are included for comparison. One is the Vanderbilt pseudopotential that we use to compute the thermal effects, denoted as pseudo-1. The other is a Rappe-Rabe-Kaxiras-Joannopoulos pseudopotential from the PWSCF website (Pt.pz-nd-rrkjus.UPF), denoted as pseudo-2. The static EOS predicted by pseudo-1 is similar to that of LAPW. Their EOS parameters differ by no more than 0.5 %. The previous overestimations of pressure are probably caused by the large cutoff radius and insufficient number of valence electrons (Ref. [2]), or another issue related to the negative electronic thermal pressure (Ref. [25]).
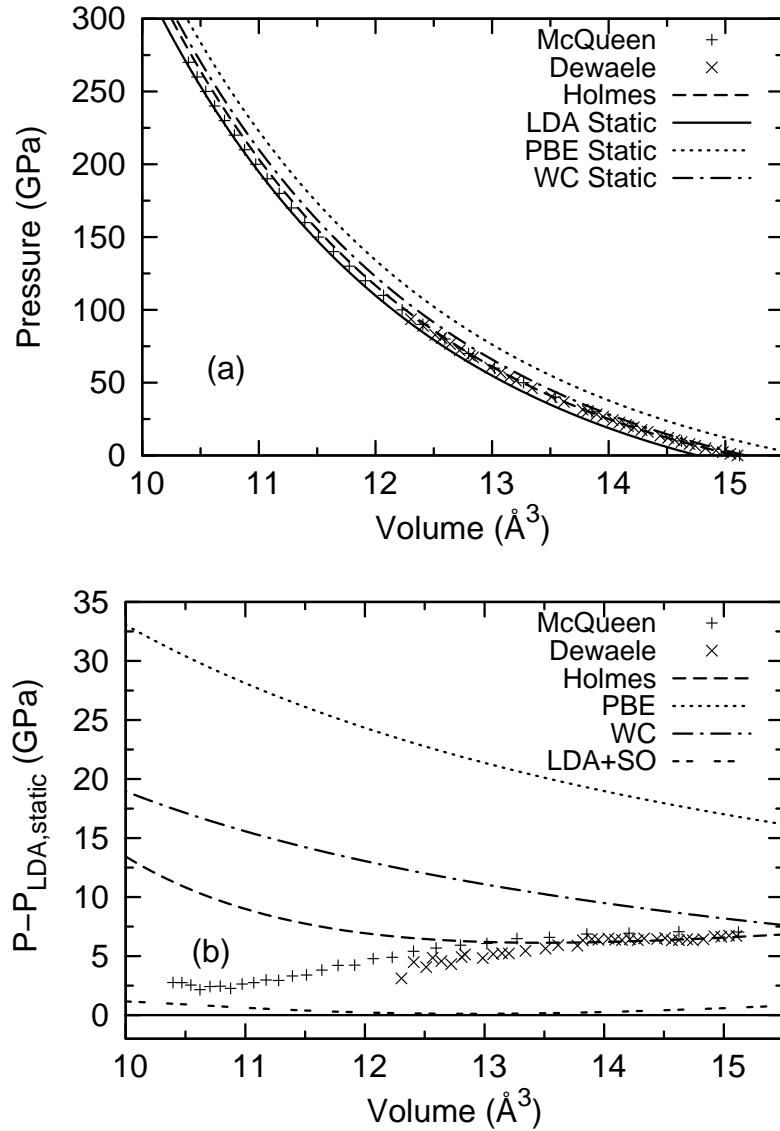
Figure 2.1: Static EOS computed by the LAPW method using various exchange correlation functionals. (a) Pressure vs. volume curves. Spin-orbit effect is too small to be identified on this scale. (b) Pressure difference with respect to the static LDA EOS. In spite of the relative large change in EOS parameters, the actual pressure difference with/without spin-orbit effect is very small. Experimental data labeled as 'McQueen' are from Ref. [5], 'Dewaele' from Ref. [3], 'Holmes' from Ref. [1].
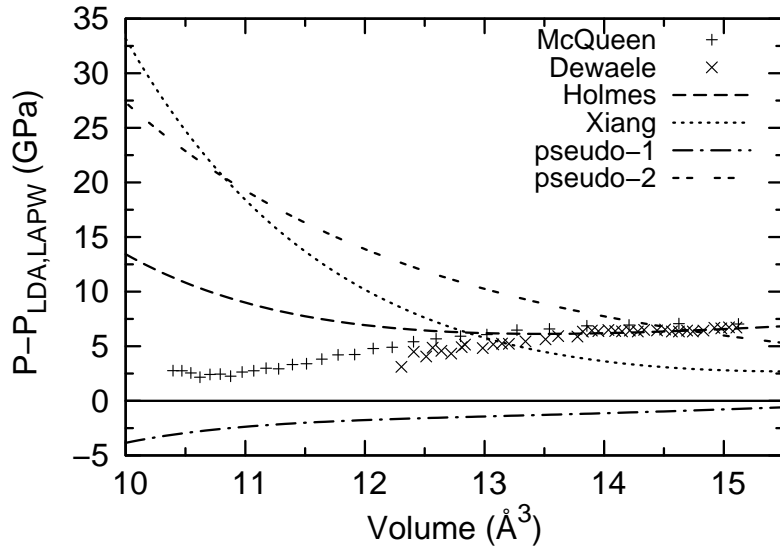
Figure 2.2: Different LDA static EOS compared with the one computed by using LAPW. 'Xiang' denotes the EOS from Ref. [25].

Platinum is a heavy element, and its electronic band structure is sensitive to spin-orbit effect.[47] We find inclusion of the spin-orbit effect increases the equilibrium volume, no matter which exchange correlation functional is used. This tendency has also been observed by Bercegeay *et al.*[43] in their pseudopotential calculations. However, the EOS parameters are not independent of each other. The variation of the equilibrium volume largely compensates that of the bulk modulus and the actual pressure difference is within 0.7 % at high pressures.

Using pseudopotentials instead of the all electron LAPW may introduce error in computing phonon frequencies, especially at high pressures. Since lattice vibrations are closely related to the force/stress on the atoms, we estimate the error in phonon frequencies by analysing the error in static pressure. At high pressures (150-550 GPa), the pressure difference between LAPW (with LDA functional) and pseudo-1 is about 1.4 %. The error in phonon frequencies caused by using pseudo-1 is likely to be of

Table 2.1: Static EOS parameters obtained from LAPW calculations and compared with those in literature. Parameters from the pseudopotential calculations (pseudo-1 and 2) are also listed. For convenience both Vinet and 4th order BM parameters are shown. V_0 denotes the equilibrium volume, K_0, K_0' and K_0'' are the isothermal bulk modulus, the first and second derivative of the bulk modulus at V_0, respectively. Note their different fitting ranges: 0-550 GPa (this study), 0-1000 GPa (Ref. [25]), 0-660 GPa (Ref. [2]), 0-150 GPa (Ref. [43]), 0-350 GPa (Ref. [39]). Ref. [43] uses 3rd order BM EOS so the corresponding K_0'' are not listed.

	Vinet			B-M			
	V_0 (Å^3)	K_0 (GPa)	K_0'	V_0 (Å^3)	K_0 (GPa)	K_0'	K_0'' (GPa^{-1})
LDA	14.752	308.02	5.446	14.761	309.29	5.295	-0.02666
LDA+SO	14.784	301.17	5.533	14.785	301.13	5.510	-0.03214
LDA(pseudo-1)	14.719	308.69	5.423	14.726	309.61	5.295	-0.02681
LDA(pseudo-2)	15.055	297.48	5.515	15.060	299.28	5.375	-0.02873
LDA[a]	14.90	300.9	5.814				
LDA[b]	15.073	293	5.56				
LDA[c](HGH)				14.82	305.99	5.32	–
LDA+SO[c,d](TM)				15.2	291.18	5.35	–
PBE	15.679	242.50	5.639	15.678	245.88	5.464	-0.03620
PBE+SO	15.751	231.97	5.762	15.754	229.96	5.850	-0.04932
PBE[a]	15.77	243.3	5.866				
PBE[c](HGH)				15.59	250.85	5.65	–
PBE[e]	15.69	248.9	5.43				
WC	15.171	280.63	5.500	15.177	283.49	5.306	-0.02889
WC+SO	15.223	269.97	5.630	15.223	269.00	5.670	-0.03893

[a]Reference [25].
[b]Reference [2].
[c]Reference [43].
[d]Reference [48].
[e]Reference [39].

the same order. Since the influence of spin-orbit effect is half of the pseudopotential uncertainty, it is ignored completely in the following calculations.

2.4.2 Phonon Dispersion and Its Electronic Temperature Dependence

Fig. 2.3 shows the phonon dispersions at the experimental ambient condition lattice constant a=7.4136 a.u..[3] One is computed at T_{ele}=0 K. The other at T_{ele}=2000 K,

close to platinum's melting point at ambient pressure 2041.3 K.[49] The Kohn anomaly (near $\mathbf{q}=[0, 0.35, 0.35]$) disappears when the electronic temperature is high, and the vibrational DOS varies noticeably. The corresponding corrections to the vibrational free energy, $\Delta F_{\mathrm{ETDV}}(V_i, T)$, are shown in Fig. 2.4 (a). ΔF_{ETDV} is always positive. As volume decreases, it diminishes and finally becomes negligible. ETDV originates in the thermal excitations of the electrons near the Fermi surface, and the number of thermal excited electrons is proportional to $N(E_{\mathrm{F}})$ in the lowest-order Sommerfeld expansion. For smaller volumes, the electronic bands are more dispersive and $N(E_{\mathrm{F}})$ decreases, as shown in Fig. 2.4(b). ETDV diminishes accordingly.

Figure 2.5 and 2.6 show the volume thermal expansion coefficient α, heat capacity at constant pressure C_P, entropy S, and the temperature-dependent part of the Gibbs free energy $\Delta G(P, T) = G(P, T) - G(P, T = 300K)$. Including ETDV removes about half of the discrepancies between experiments and calculations based on normal QHA. The remaining small differences between theory and experiment are attributed to anharmonic phonon-phonon interactions[50] and electron-phonon interactions.[51] These two effects are of the same order of magnitude[51] as F_{ele} for metals, but explicit perturbative calculations to determine their magnitudes are computational demanding and beyond the scope of the current paper. We notice DFT calculations based on QHA describe well the thermal properties of other metals, such as gold,[41] silver,[52] copper,[53] up to melting point. This is in contrast with ionic crystals like MgO, where there are large deviations from QHA at high temperatures. It is possible that the effects of anharmonic phonon-phonon interaction and electron-phonon interaction tend to cancel each other in these metals. Further work is needed to clarify this issue.
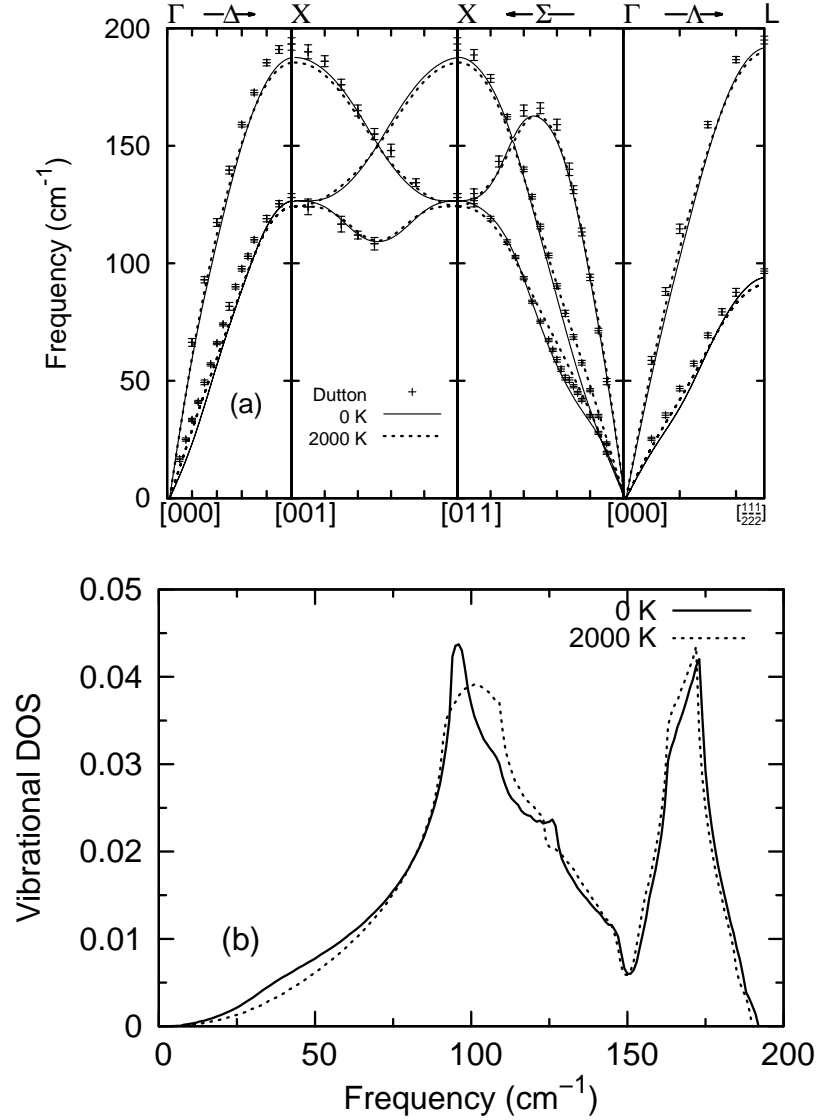
Figure 2.3: (a) Phonon dispersion and (b) vibrational DOS at a=7.4136 a.u.. Solid line corresponds to T_{ele}=0 K, dashed line corresponds to T_{ele}=2000 K. They are calculated by using the LDA pseudopotential. Experimental data labeled as 'Dutton' are from Ref. [28].
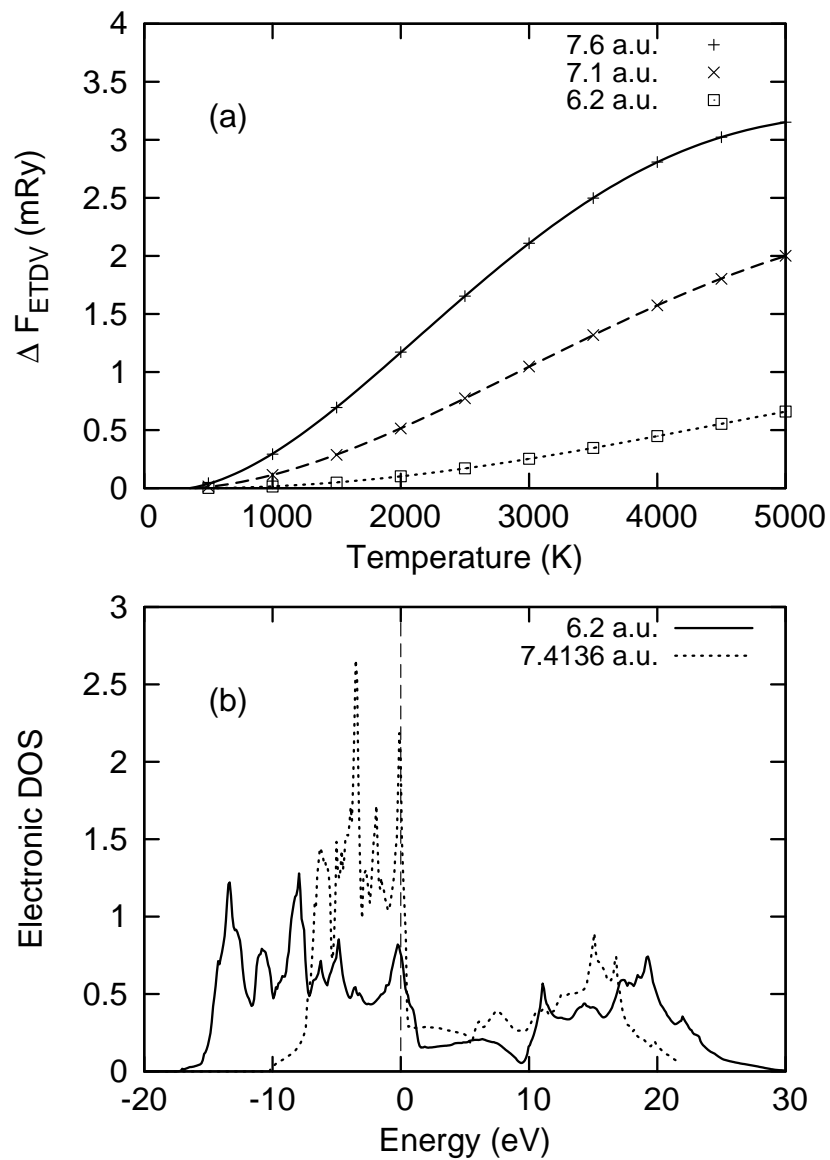
Figure 2.4: (a) Corrections to the vibrational free-energy at various lattice constants.
(b) Volume dependence of the electronic density of states.
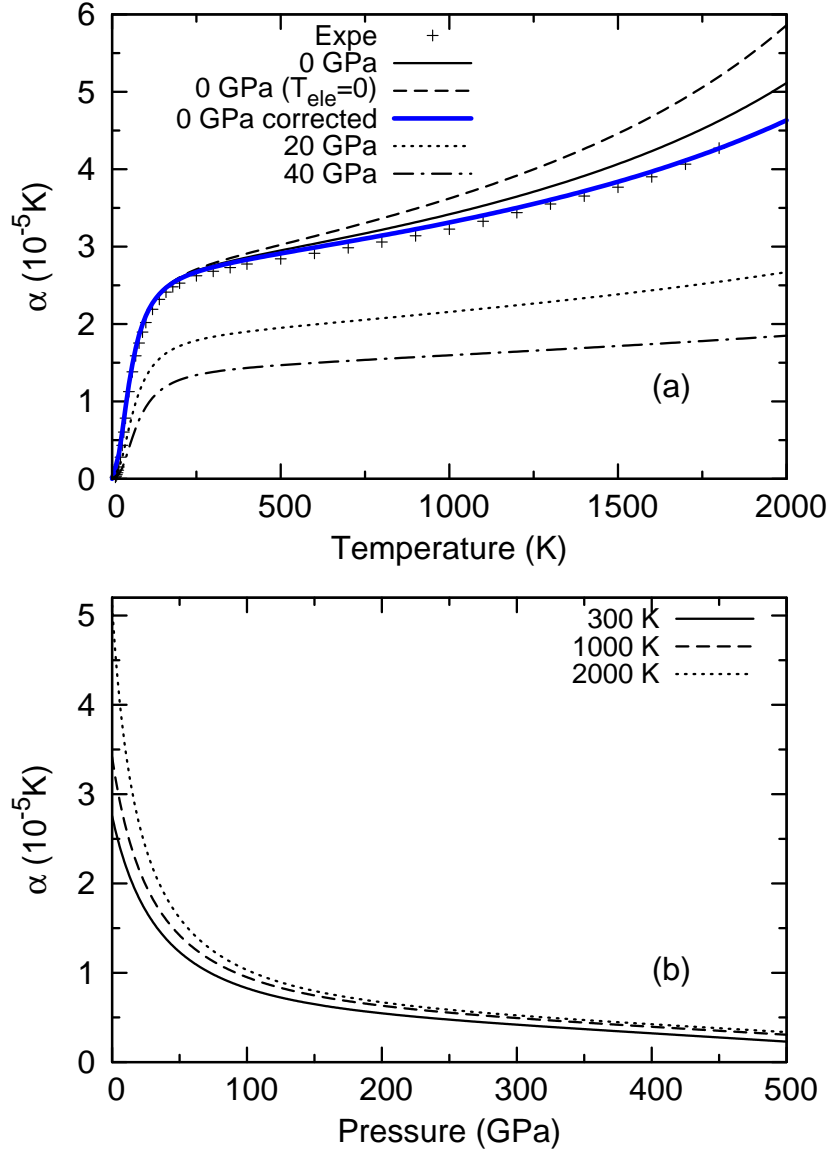
Figure 2.5: Thermal expansivity as a function of (a) temperature and (b) pressure. Curves with label '($T_{ele}=0$)' represent properties computed without ETDV, i.e. computed from F_{vib}^{QHA}. Curves without this specification are the default ones computed with ETDV. '0 GPa corrected' denotes the results obtained by adding a phenomenological correction to account for anharmonic phonon-phonon interactions and electron-phonon interactions. These corrected thermal data are used to construct the final thermal EOS in Table 2.3 and 2.4. The experimental data are from Ref. [54].
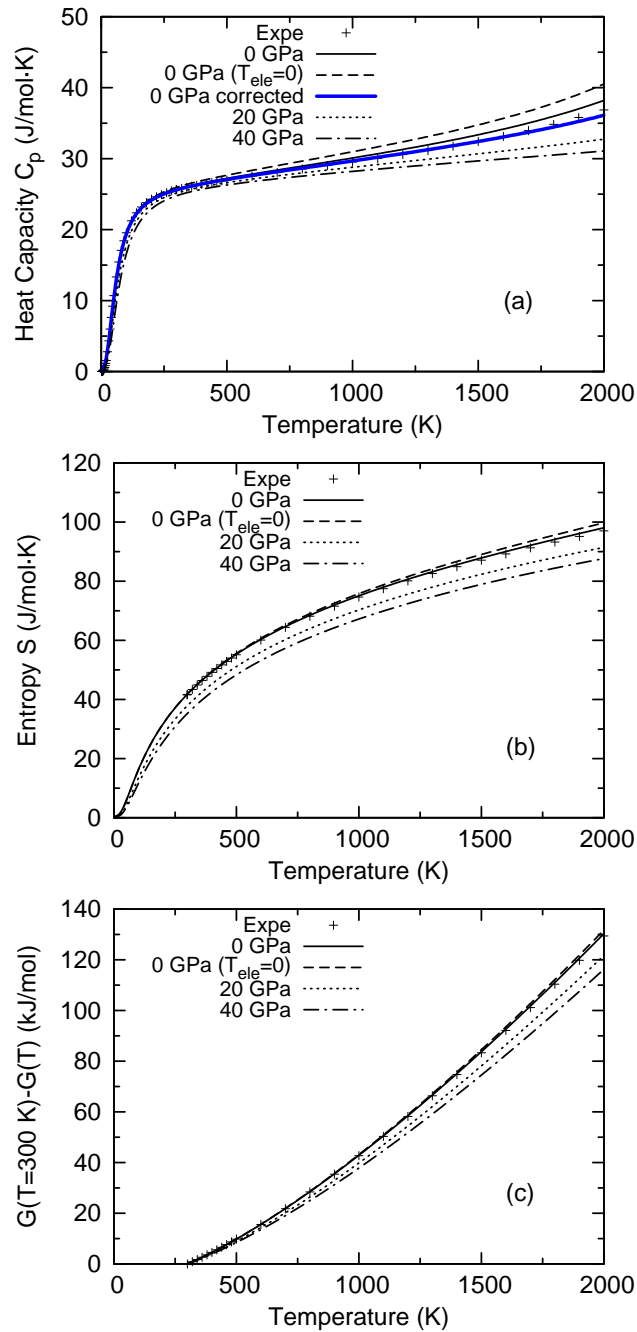
Figure 2.6: Thermal properties of platinum. (a) Heat Capacity at constant pressure, (b) Entropy, (c) Temperature dependence of the Gibbs free energy at constant pressure. The meanings of the labels are the same as above. On this scale it is difficult to discern the improvements on entropy and Gibbs free energy, caused by including the phenomenological correction on anharmonic phonon-phonon interactions and electron-phonon interactions. Thus those data are not shown. The experimental data are from Ref. [55].

2.4.3 Room Temperature Isotherms

By fitting the total Helmholtz free energy at 300 K, we get the theoretical 300 K isotherms, as shown in Fig. 2.7. Their parameters are listed in Table 2.2. In the low pressure range, the LDA isotherm and the experimental data are almost parallel. As pressure increases, they start to merge. It seems LDA works better at high pressures. Regarding to EOS parameters, LDA gives equilibrium volumes closest to the experiments, WC yields closest bulk modulus (K_0) and the derivative of the bulk modulus (K_0'). Some people[3, 43] prefer to compare pressures from two EOS (labeled as EOS-I and EOS-II) at the same compression, i.e. the same value of V/V_0. V_0 is the corresponding equilibrium volume, $V_{0,\mathrm{I}}$ for EOS-I, $V_{0,\mathrm{II}}$ for EOS-II. Such comparisons can give favorable agreement when K_0 and K_0' of EOS-I are close to those of EOS-II, even $V_{0,\mathrm{I}}$ and $V_{0,\mathrm{II}}$ are quite different.[3] As mentioned before, the EOS parameters are not independent of each other. It can be fortuitous that K_0 and K_0' agree well. Judged from pressure vs. volume relation, LDA is the optimal functional for platinum. It is worth noting the LDA (HGH) pressure vs. volume relation reported in Ref. [43] is similar to those obtained in this study. However, Ref. [43] presents data in volume vs. compression, and concludes LDA overestimates pressure by 8 GPa near 100 GPa. In fact, although $K_{0,\mathrm{LDA}}$ (291 GPa from this study) is much larger than $K_{0,\mathrm{expe}}$ (273.6 GPa from Ref. [3]), the bulk modulus computed at the experimental equilibrium volume $V_{0,\mathrm{expe}}$ (15.095 Å^3) is 270 GPa, quite close to $K_{0,\mathrm{expe}}$. Thus when plotted in pressure vs. volume, the isotherm computed by LDA is nearly parallel with the experimental data in the low pressure range.
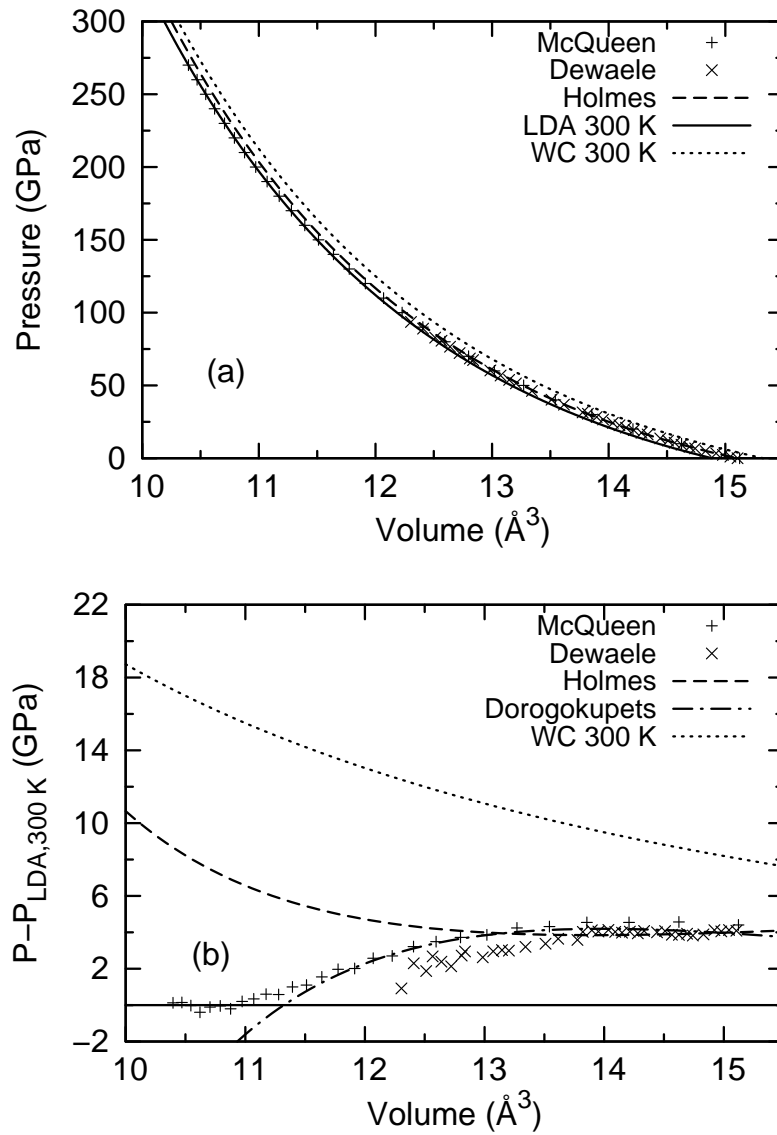
Figure 2.7: 300 K isotherms. (a) pressure vs. volume. (b) pressure difference. 'Dorogokupets' denotes EOS from Ref. [4], which is very close to the reduced shock EOS (McQueen) near 100 GPa. PBE is not plotted as its EOS is way off.

Table 2.2: EOS parameters of the theoretical 300 K isotherms, compared with the experiments. $V_{0,\text{expe}}$ is 15.095 Å^3. Pressure range: 0-550 GPa (this study), 0-660 GPa (Ref. [1] and [2]), 0-94 GPa (Ref. [3] and [4]), 0-270 GPa (Ref. [5]).

	Vinet			B-M			
	V_0 (Å^3)	K_0 (GPa)	K_0'	V_0 (Å^3)	K_0 (GPa)	K_0'	K_0'' (GPa^{-1})
LDA	14.884	291.25	5.547	14.886	291.65	5.496	-0.03232
LDA ($V_{0,\text{expe}}$)		269.96	5.640		269.91	5.626	-0.03730
LDA[a]	15.188	281	5.61				
PBE	15.864	225.55	5.751	15.866	225.34	5.741	-0.04709
WC	15.322	263.93	5.601	15.325	264.72	5.530	-0.03580
Holmes[b]	15.10	266	5.81				
Dewaele[c]	15.095	273.6	5.23				
Dorogokupets[d]	15.095	276.07	5.30				
McQueen[e]				15.123	277.715	4.821	-0.01379

[a]Reference [2].

[b]Reference [1].

[c]Reference [3]. When K_0 is set to 277 GPa, the value measured by ultrasonic experiments, K_0' equals 5.08 GPa.

[d]Reference [4], improved analysis using data from Ref. [3].

[e]Reference [5], Fitted from the tabulated shock reduced isotherm at 293 K.

2.4.4 Thermal EOS of Platinum for Pressure Calibration

In the previous sections the thermal properties of platinum is discussed from a pure theoretical point of view. We have computed the static lattice energy $U(V)$ using LAPW, and found spin-orbit interactions are not important in determining the EOS of platinum. We have used QHA to calculate the vibrational free energy $F_{\text{vib}}(V, T)$, and found including ETDV improves the agreement on the thermal properties. We have calculated the electronic free energy $F_{\text{ele}}(V, T)$ using Mermin functional. The resulting thermal properties, e.g. the temperature-dependent part of the Gibbs energy $\Delta G(P, T)$, are close to the experimental data at 0 GPa, The room temperature isotherm computed by LDA merges to the reduced shock data at high pressures, indicating LDA works better at high pressures.

Based on these DFT results and all the available experimental data, we try to

construct a consistent P-V-T EOS of platinum up to 550 GPa and 5000 K. To reach this goal, first we need to include the physical effects which are missing in our original model. A phenomenological term[46] $\Delta F_{\text{corr}}(V,T) = -\frac{3}{2}k_{\text{B}}a(V/V_0)^m T^2$ is added to the total Helmholtz energy to account for the anharmonic phonon-phonon interactions and electron-phonon interactions, where V_0 is the volume of a primitive cell at ambient condition ($V_0 = 15.095$ Å^3). The quadratic temperature dependence comes from the lowest order perturbation at high temperatures. a and m are two parameters to be fitted. We find setting a equals 10^{-5} K^{-1}, m equals 7 yields good agreement between theory and experiments on α, C_P and $\Delta G(P,T)$ at 0 GPa, as illustrated in Figs. 2.5(a) and 2.6(a). The contribution to thermal pressure can be estimated by differentiating $\Delta F_{\text{corr}}(V,T)$ with respect to volume. At 2000 K, ΔP_{th} is 0.38 GPa when V equals V_0, 0.2 GPa when V equals $0.9V_0$.

Having obtained accurate $\Delta G(P,T)$, the next step is to get reliable $G(P, 300 \text{ K})$. We choose the room temperature EOS developed by Dorogokupets *et al.*[4] as our reference below 100 GPa. It has been cross checked with other pressure scales, and is likely to be more accurate than the reduced shock data of Ref. [5] in this pressure range. On the other hand, extrapolating an EOS fitted at low pressures to higher range can be dangerous. We assume LDA works better at high pressures, and the difference between the exact (obtained in an ideal, very accurate experiment) and LDA isotherm approaches to zero as pressure increases.

We compare Dorogokupets's EOS[4] (V_0=15.095 Å^3, K_0=276.07 GPa, K_0'=5.30 in Vinet form) with our room temperature isotherm computed by LDA (V_0=14.884 Å^3, K_0=291.25 GPa, K_0'=5.547 in Vinet form). The volume difference between these two at each pressure $\Delta V(P) = V_{\text{expe,300 K}}(P) - V_{\text{LDA,300 K}}(P)$ is shown in Fig. 2.8. Since $\Delta V(P)$ decreases rapidly as pressure increases, we use exponentially decaying
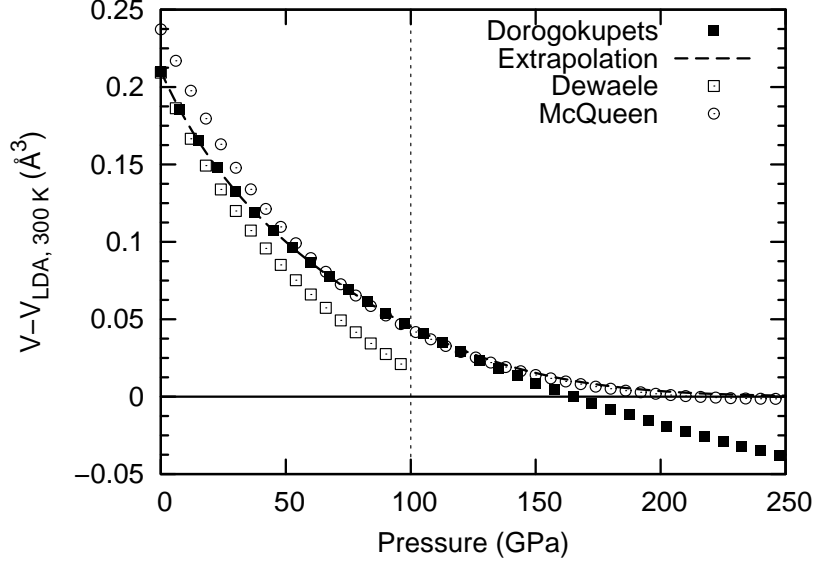
Figure 2.8: Volume Correction to the theoretical isotherm at 300 K. We use $\Delta V(P) = 0.1215 \cdot \exp(-P/34.0846) + 0.0885 \cdot \exp(-(P/109.989)^2)$ to fit the volume difference in the range $P < 100$ GPa. The exponential functional form guarantees that it approaches zero at high pressures. It happens that this extrapolation agrees well with McQueen's reduced shock data.

functions to fit and extrapolate. We correct the calculated room temperature Gibbs energy $G_{\mathrm{LDA}}(P, 300 \text{ K})$ by setting $G_{\mathrm{corr}}(P, 300 \text{ K}) = G_{\mathrm{LDA}}(P, 300 \text{ K}) + \int_0^P \Delta V(P) dP$. The isotherm derived from $G_{\mathrm{corr}}(P, 300 \text{ K})$ coincides with Dorogokupets' EOS below 100 GPa. the upper limit of their fitting. Above 250 GPa, $\Delta V(P)$ is almost zero, and the isotherm derived from $G_{\mathrm{corr}}(P, 300 \text{ K})$ is the same as the uncorrected one. The uncertainty due to volume extrapolation in the intermediate region (100 GPa to 250 GPa) is estimated from bulk modulus to be less than 1 GPa. It is worth noting that the established EOS of platinum are quite quite similar to each other below 100 GPa, as shown in Fig. 2.7(b). Choosing a different reference such as the one in Ref. [3] will only change the results near 100 GPa by 1 GPa.

We combine $G_{\mathrm{corr}}(P, 300 \text{ K})$ with the temperature-dependent part of the Gibbs

energy $\Delta G(P,T)$, and get the corrected Gibbs energy $G_{\text{corr}}(P,T)$ at temperature T. From $G_{\text{corr}}(P,T)$ we derive all the other thermodynamical properties. Thermal properties like α, C_P, S, which depend on the temperature derivatives of the Gibbs energy, are not affected by changing $G(P, 300\text{ K})$. In contrast, the isothermal bulk modulus K_T and adiabatic bulk modulus K_S will be influenced, as shown in Fig. 2.9.

After corrections, both thermal expansivity and bulk modulus agree with the experiments well. We expect the product αK_T to be accurate. Integrating αK_T we get the thermal pressure, $P_{\text{th}}(V,T) = P(V,T) - P(V,T_0) = \int_{T_0}^{T} \alpha K_T dT$. The calculated αK_T and P_{th}, before and after corrections, are shown in Fig. 2.10. $P_{\text{th}}(V,T)$ is often assumed to be independent of volume and linear in temperature, i.e. αK_T is a constant. Ref. [5] assumes the thermal energy $E(T) = 3k_B T$, the thermal Grüneisen parameter $\gamma = \gamma_0 V/V_0$, where γ_0=2.4, and V_0=15.123 Å^3. The thermal pressure is obtained from Mie-Grüneisen relation

$$P_{\text{th}}(V,T) = \frac{E(T)\gamma(V)}{V} = \frac{3k_B\gamma_0}{V_0} \cdot T = 6.57 \times 10^{-3} \cdot T \text{ (GPa)}. \qquad (2.5)$$

In Ref. [1], αK_T is estimated to be 6.94×10^{-3} GPa/K. Both values lie within the variation of the calculated αK_T, as shown in Fig. 2.10(a). We find that αK_T (P_{th}) has noticeable volume dependence. At fixed temperature, it first decreases, reaches a minimum at about $V/V_0 = 0.8$, then increases. Such behavior originates in the pressure dependence of the thermal expansivity (Fig. 2.5(b)) and bulk moduli (Fig. 2.9(b)). This feature has also been observed in Ref. [4], as shown in Fig. 2.10(b). However it is missing in the previous *ab initio* calculation.[25]

Thermal Grüneisen parameter $\gamma = \frac{\alpha K_T V}{C_V}$ is an important quantity. Empirically it is often assumed to be independent of temperature. Its volume dependence is
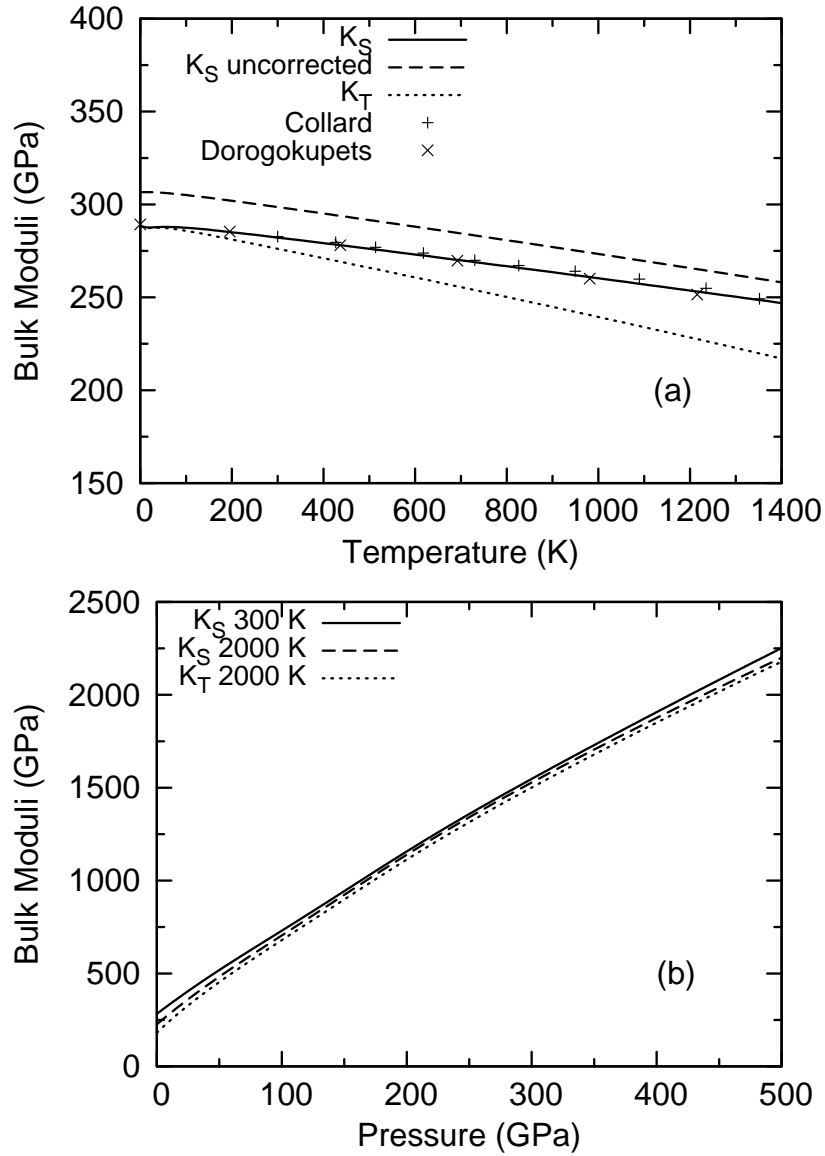
Figure 2.9: (a) Bulk moduli at 0 GPa. 'Uncorrected' denotes the raw DFT results without any correction. As noted in Ref. [4], the experimental data in Ref. [56] is inconsistent. The data points we show here are digitized from the graphs in Ref. [56] (denoted as 'Collard') and [4] (denoted as 'Dorogokupets') respectively. K_S deduced from the corrected Gibbs free energy agrees well with the one computed from empirical models in Ref. [4]. (b) Bulk moduli as a function of pressure.
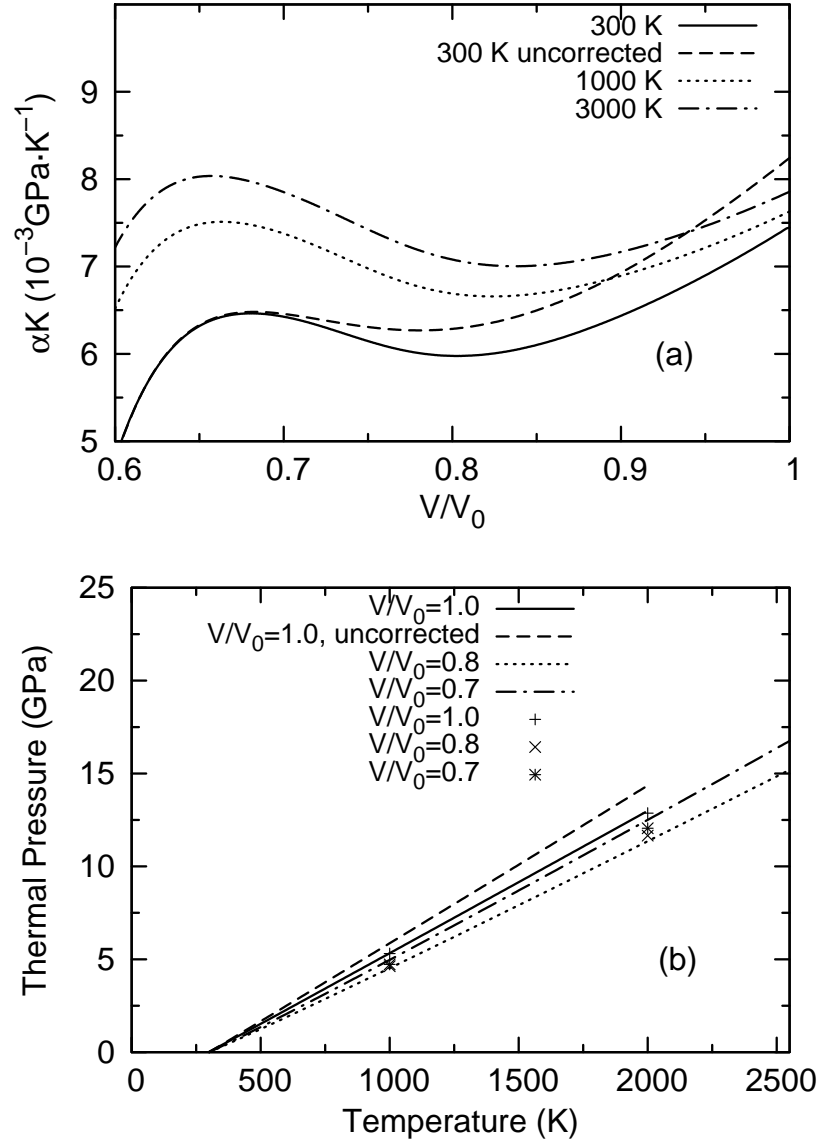
Figure 2.10: (a) temperature derivative of P_{th}, $\alpha K_T = \frac{\partial P_{\text{th}}}{\partial T}$ before/after corrections. (b) Thermal pressure P_{th} at different V/V_0, where V_0 is the experimental volume at ambient condition (15.095 Å^3). Points are the thermal pressures from Ref. [4].

described by a parameter $q=\frac{\partial \ln \gamma}{\partial \ln V}$, and γ can be represented in q as $\gamma = \gamma_0 \left(\frac{V}{V_0}\right)^q$. From Mie-Grüneisen relation, it is obvious that q is related to the volume dependence of αK_T. If q equals 1, αK_T is independent of volume. If q is greater than 1, αK_T gets smaller as volume decreases. In Ref. [5] q is assumed to equal 1. Fei *et al.*[23] determined γ by fitting the measured P-V-T data to the Mie-Grüneisen relation up to 27 GPa. They gave γ_0=2.72 and q=0.5. Zha *et al.*[24] extended measurements to 80 GPa and 1900 K. Their fit gave γ_0=2.75 and q=0.25. Our calculation indicates that the temperature dependence of γ is small. The volume dependence of γ is shown in Fig. 2.11. The uncorrected DFT calculation tends to overestimate γ. At ambient condition γ_0 equals 2.87. After corrections, γ_0=2.70. The corresponding q equals 2.35, much larger than the value obtained in Ref. [23] and [24]. We notice previous DFT calculation on gold[41] also gives much larger q than the value in Ref. [23]. This is probably due to the small pressure range explored in Ref. [23], and limited number of data points measured in Ref. [24].

Adding the thermal pressure to the room temperature isotherm, we get the thermal EOS of platinum, as shown in Table 2.3. We compare our results with two DAC measurements in Fig. 2.12. Within the error of the experiments, the agreement is reasonably good. For convenience of interpolation, parametric forms of the thermal EOS are listed in Table 2.4.

The P-V-T thermal EOS we obtained are very similar to the one in Ref. [4] below 100 GPa, This is expectable as we used the 300 K isotherm in Ref. [4] as the reference to correct the room temperature Gibbs energy, and the thermal properties calculated from both approaches agree well with the experiments. In this P-T range, the uncertainty of our EOS is comparable to the one in Ref. [4] . Above 100 GPa, the uncertainty is about 1.4 %, which is difference between the LAPW (LDA) and
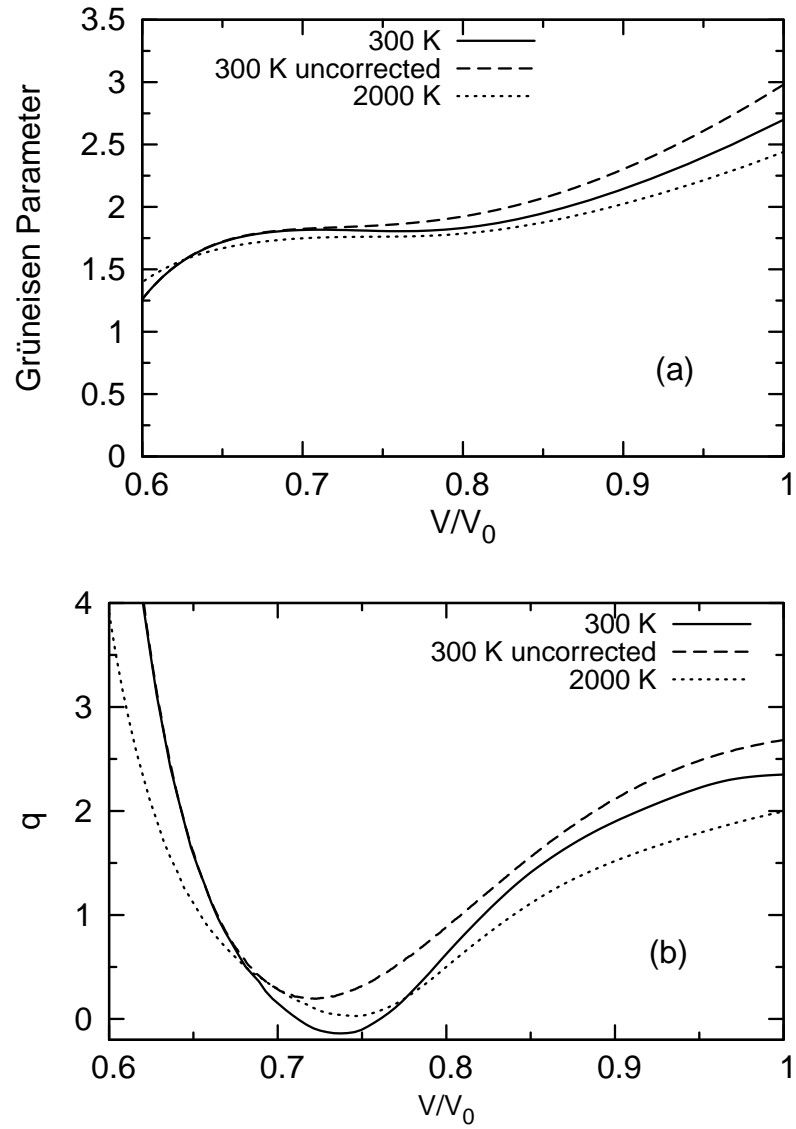
Figure 2.11: Thermal Grüneisen parameter (a) volume dependence at fixed temperature; (b) the corresponding q.

Table 2.3: Pressure (in GPa) as a function of compression (1-V/V_0, V_0 is the experimental volume at ambient condition. 15.095 Å^3) and temperature (in K), deduced from the corrected Gibbs free energy. Pressures above melting point is not shown. The melting point is determined using $T_m(P) = 2057 + 27.2 \times P - 0.1497 \times P^2$ K up to 70 GPa from Ref. [49]

$1 - V/V_0$	300	500	1000	1500	2000	2500	3000	3500
0.00	0.00	1.51	5.31	9.14	12.97			
0.05	16.22	17.62	21.20	24.83	28.48	32.16		
0.10	38.32	39.64	43.05	46.52	50.03	53.57	57.14	
0.15	68.41	69.67	72.97	76.34	79.77	83.24	86.73	90.25
0.20	109.46	110.71	113.99	117.37	120.82	124.31	127.83	131.39
0.25	166.45	167.74	171.15	174.69	178.29	181.94	185.63	189.36
0.30	247.37	248.72	252.34	256.07	259.88	263.73	267.64	271.58
0.35	362.30	363.65	367.31	371.10	374.98	378.91	382.90	386.94
0.40	525.86	526.93	530.04	533.39	536.86	540.40	543.99	547.62

pseudo-1 static EOS. Other sources of error, e.g. convergence uncertainty (0.5 %) and ignoring spin-orbit effect (0.7 %) are smaller effects. To check the accuracy of our thermal EOS at high pressures, we start from the corrected Gibbs energy and compute the theoretical Hugoniot by solving the Rankine-Hugoniot equation:

$$E_H(V,T) - E_i(V_0, T_i) = (P_H(V,T) + P_0(V_0, T_i)) \frac{V_0 - V}{2}, \qquad (2.6)$$

where $E_H(V,T)$, $P_H(V,T)$ are the internal energy, pressure at volume V and temperature T. $E_i(V_0, T_i)$, $P_0(V_0, T_i)$ are the internal energy, pressure at the initial volume V_0 and temperature T_i. The results are shown in Fig. 2.13. The predicted Hugoniot pressure is in good agreement with measurements. The temperature predicted by DFT is lower than the empirically deduced value in Ref. [5]. The reduction in Ref. [5] neglects the electronic thermal pressure, and this may cause overestimating Hugoniot temperature.[1]

We end this section by comparing our room temperature isotherm with that of Holmes *et al.*. Below 70 GPa, they are almost identical. At high pressures (200-550 GPa), the pressure from our EOS is about 3 % lower than the one from Holmes *et al.*. Holmes *et al.* used LMTO with the atomic-sphere approximation to get the static EOS. In principle, the full potential LAPW method used in this study is more accurate. It seems the EOS of Holmes *et al.* overestimates pressure systematically at high compression ratio. But the magnitude is much smaller than the pressure offset needed to compensate the discrepancy between Mao *et al.*'s experiment and seismological extrapolation. The real cause of the discrepancy might be a combination of several factors.

2.5   Conclusions

In this paper, we report our calculations on the static and thermal EOS of platinum using DFT with different exchange correlation functionals. Contrary to previous reports, we find the room temperature isotherm computed with LDA lies below, and nearly parallel to the experimental compression data. We study the lattice dynamics of platinum within QHA, and find the electronic temperature dependence of vibrations plays a noticeable role in determining the thermal properties of platinum. Combining the experimental data with DFT calculations, we propose a consistent thermal EOS of platinum, up to 550 GPa and 5000 K, which can be used as a reference for pressure calibration.
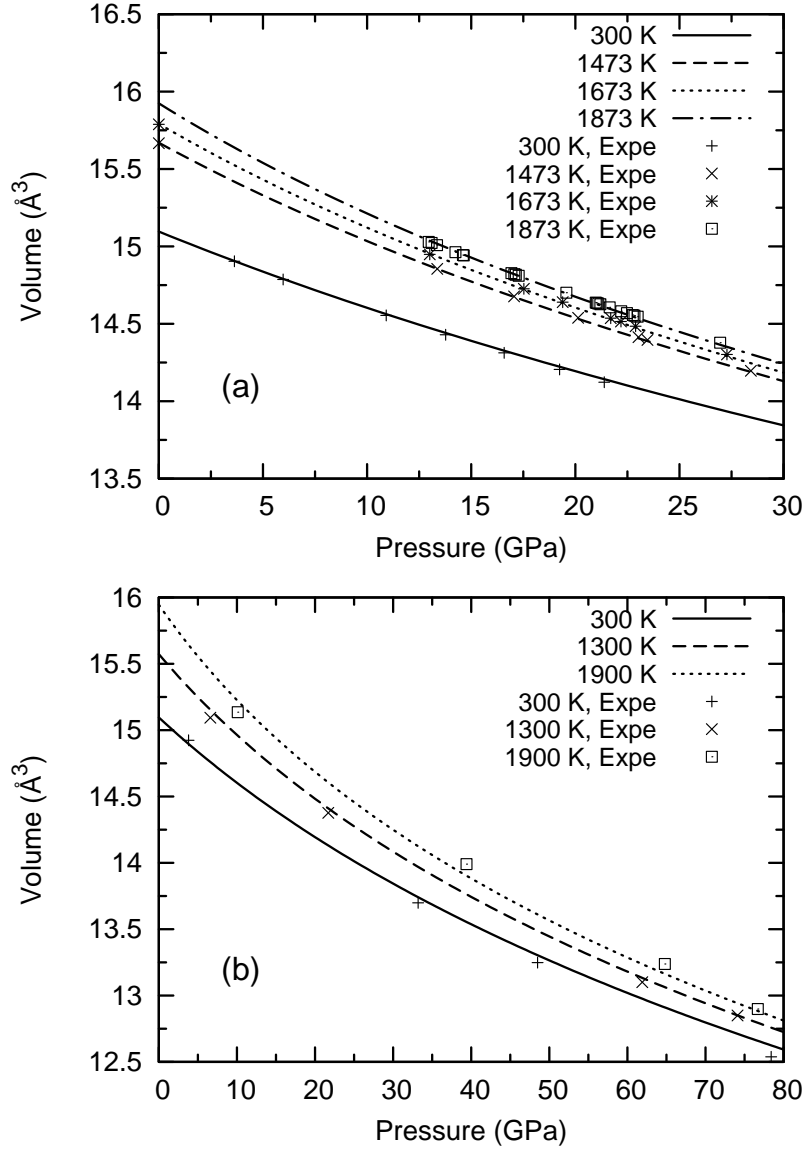
Figure 2.12: High temperature isotherms after corrections. Lines correspond to the calculated isotherms. The experimental data in (a) are taken from Ref. [27], except those at $P{=}0$ GPa, which are obtained by integrating the thermal expansivity listed in Ref. [54]. Data in (b) are from Ref. [24].

Table 2.4: Parametric form of the thermal EOS, $P(V)=P_0+\frac{3}{2}K_0\left[(V/V_0)^{-\frac{7}{3}}-(V/V_0)^{-\frac{5}{3}}\right]$ $\cdot\left\{1+\frac{3}{4}(K_0'-4)[(V/V_0)^{-\frac{2}{3}}-1]+\frac{3}{8}[K_0K_0''+(K_0'-3)(K_0'-4)+\frac{35}{9}][(V/V_0)^{-\frac{2}{3}}-1]^2\right\}$. At high temperatures, the equilibrium volume may exceed the largest volume we calculate. For better accuracy we fit the P-V-T data in three different pressure-temperature intervals: (1) 0-100 GPa and 0-2000 K, (2) 50-250 GPa and 0-3000 K, (3) 150-550 GPa and 0-5000 K. P_0 denotes the starting pressure of the corresponding interval. V_0, K_0, K_0', and K_0'' are temperature dependent parameters, and are fitted to a 4th order polynomial $a_0+a_1t+a_2t^2+a_3t^3+a_4t^4$, where $t=T/1000$. They have a formal correspondence to the usual 4th order BM EOS parameters, which are defined at $P_0=0$ GPa.

(1)	a_0	a_1	a_2	a_3	a_4
$V_0(\text{Å}^3)$	14.9924	0.295837	0.194441	-0.0917141	0.024365
$K_0(\text{GPa})$	290.539	-45.4082	-9.38792	5.09573	-1.40266
K_0'	5.11956	0.52903	0.0733263	-0.0195011	0.0229666
$K_0''(\text{GPa}^{-1})$	-0.0275729	-0.0120014	-0.0114928	0.00672243	-0.00359317
(2)	a_0	a_1	a_2	a_3	a_4
$V_0(\text{Å}^3)$	13.2246	0.128227	0.049052	-0.0160359	0.00241857
$K_0(\text{GPa})$	523.48	-30.3849	-3.86087	1.31313	-0.222027
K_0'	4.24183	0.217262	-0.0235333	0.00944835	-0.000371746
$K_0''(\text{GPa}^{-1})$	-0.00125873	-0.00268918	2.13874e-05	-3.57657e-05	-1.75847e-05
(3)	a_0	a_1	a_2	a_3	a_4
$V_0(\text{Å}^3)$	11.4929	0.0672156	0.0119585	-0.00243269	0.000219022
$K_0(\text{GPa})$	951.004	-21.0874	-2.84254	0.654708	-0.0639296
K_0'	4.31383	0.05775	-0.00505386	0.00245414	-0.000167453
$K_0''(\text{GPa}^{-1})$	-0.00588145	-0.00130468	0.000221904	-6.51359e-05	4.99978e-06
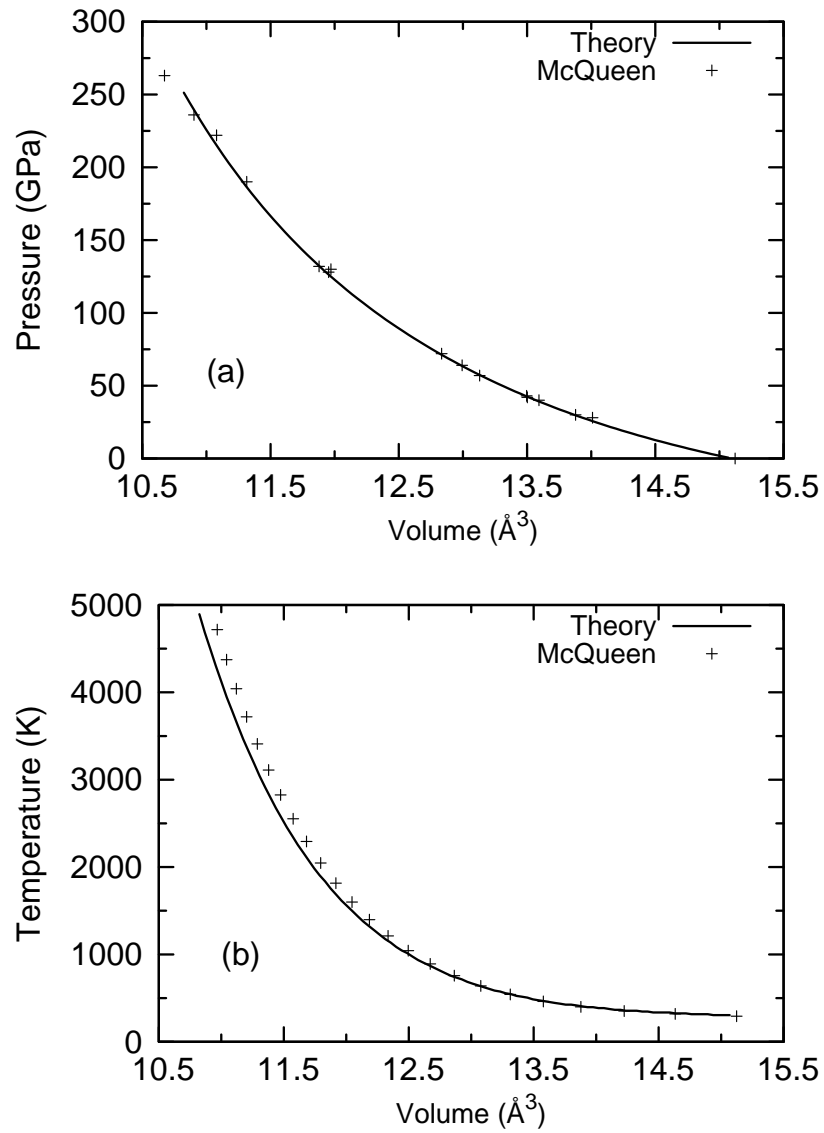
Figure 2.13: (a) Theoretical shock Hugoniot compared with the expermental data from McQueen *et al.* (Ref. [5]). (b) Temperature along the Hugoniot.

Chapter 3

Preliminaries on Infrared Properties

3.1   Macroscopic Description

Knowing the optical properties of the minerals is useful. At the temperature and pressure of the Earth's lower mantle, heat can be conducted by both phonons (vibrational heat conductivity) and photons (radiative heat conductivity). The radiative heat conductivity is directly related to the optical properties of the minerals. On the other hand, optical spectroscopy is a powerful and convenient tool to study the elementary excitations of the materials. In particular, infrared spectroscopy can provides a lot of information on lattice vibrations.

Table 3.1: Interrelation among commonly used optical parameters.

Conductivity	$\sigma = \sigma_1 + i\sigma_2$
Dielectric Function	$\epsilon = \epsilon_1 + \epsilon_2, \ \epsilon = 1 + \frac{4\pi i\sigma}{\omega},$
	$\epsilon_1 = 1 - \frac{4\pi\sigma_2}{\omega}, \ \epsilon_2 = \frac{4\pi\sigma_1}{\omega}$
Refractive Index	$N = n + ik, \ \epsilon = N^2, \ \epsilon_1 = n^2 - k^2, \ \epsilon_2 = 2nk$
	$n^2 = (\epsilon_1 + \sqrt{\epsilon_1^2 + \epsilon_2^2})/2, \ k^2 = (-\epsilon_1 + \sqrt{\epsilon_1^2 + \epsilon_2^2})/2$
Absorption Coefficient	$\alpha(\omega) = 2\omega k/c = \omega\epsilon_2/nc$
Reflectivity	$r\exp(i\Delta) = (1 - \sqrt{\epsilon})/(1 + \sqrt{\epsilon}) = (1 - n - ik)/(1 + n + ik),$
	$R = \frac{(n-1)^2 + k^2}{(n+1)^2 + k^2}, \ \tan\Delta = \frac{2k}{n^2 + k^2 - 1}$ (at normal incidence)

How light interact with materials is described by Maxwell's Equations[57]

$$\begin{cases} \nabla \cdot \mathbf{D} = 0 \\[6pt] \nabla \cdot \mathbf{B} = 0 \\[6pt] \nabla \times \mathbf{E} = -\frac{1}{c}\frac{\partial \mathbf{B}}{\partial t} \\[6pt] \nabla \times \mathbf{H} = \frac{1}{c}\frac{\partial \mathbf{D}}{\partial t}, \end{cases} \tag{3.1}$$

where the electric displacement $\mathbf{D} = \epsilon\mathbf{E}$. The dielectric function ϵ is a frequency dependent complex function and contains all the information needed to describe the optical response of the material. By solving Maxwell's equations with boundary conditions resembling the experimental setup, we can connect the dielectric function $\epsilon(\omega)$ with the experimentally measurable quantities, such as reflectivity $R(\omega)$ and absorption coefficient $\alpha(\omega)$. Table 3.1 summarizes the interrelation among typical parameters describing the optical properties of the material.

The real and imaginary part of the dielectric function are connected by the

Kramers-Kronig relations[57]

$$\begin{cases} \epsilon_1(\omega) = 1 + \frac{2}{\pi} P \int_0^{+\infty} \frac{\omega' \epsilon_2(\omega')}{\omega'^2 - \omega^2} d\omega' \\ \epsilon_2(\omega) = -\frac{2\omega}{\pi} P \int_0^{+\infty} \frac{\epsilon_1(\omega') - 1}{\omega'^2 - \omega^2} d\omega'. \end{cases} \qquad (3.2)$$

A similar relation exists between the modulus $\frac{1}{2} \ln(R)$ and phase Δ of the reflectivity

$$\Delta(\omega) = \frac{2\omega}{\pi} \int_0^{+\infty} \frac{\frac{1}{2} \ln R(\omega')}{\omega^2 - \omega'^2}. \qquad (3.3)$$

The modulus of the reflectivity $R(\omega)$ is measured experimentally from a Fourier transform infrared spectrometer (FTIR). Its phase $\Delta(\omega)$ is determined by Eq. (3.3). The dielectric function $\epsilon(\omega)$ and other optical functions are computed by using the formula listed in Table 3.1.

3.2 Linear Response Theory

The microscopic theory of the dielectric function is an example of linear response theory. Let $\mathbf{H_0}$ be the Hamiltonian of the crystal lattice without external electric field, ρ_0 be the corresponding density matrix. In thermal equilibrium, ρ_0 is independent of time. With a time-dependent interaction $\mathbf{H_I}$, the density matrix $\rho(t)$, which has a similar role as the distribution function in classical statistical mechanics, evolves according to the quantum Liouville equation:

$$i\hbar\dot{\rho} = [\mathbf{H}(t), \rho(t)] \qquad (3.4)$$

If we assume at $t = -\infty$ the system is the thermal equilibrium and $\mathbf{H_I}$ is turned later, we can obtain a formal solution for $\rho(t)$ as

$$\rho(t) = \rho_0 + \frac{1}{i\hbar} \int_{-\infty}^{t} [\mathbf{H}(t'), \rho(t')] dt' \qquad (3.5)$$

The first order iterative solution replaces $\rho(t')$ in the time integration by ρ_0. Taking into account $[\mathbf{H_0}, \rho_0] = 0$, we get

$$\rho(t) = \rho_0 + \frac{1}{i\hbar} \int_{-\infty}^{t} [\mathbf{H_I}(t'), \rho_0] dt' \qquad (3.6)$$

For an arbitrary quantum variable $\mathbf{A}(t)$, its ensemble average is $\langle \mathbf{A} \rangle = \mathrm{tr}(\rho \mathbf{A})$. The presence of $\mathbf{H_I}$ causes

$$
\begin{aligned}
\delta \langle A \rangle &= \frac{1}{i\hbar} \int_{-\infty}^{t} \mathrm{tr}\left([\mathbf{H_I}(t'), \rho_0] \mathbf{A}(t)\right) dt' \\
&= \frac{1}{i\hbar} \int_{-\infty}^{t} \mathrm{tr}\left(\rho_0 [\mathbf{A}(t), \mathbf{H_I}(t')]\right) dt' \\
&= \frac{1}{i\hbar} \int_{-\infty}^{t} \langle [\mathbf{A}(t), \mathbf{H_I}(t')] \rangle dt'.
\end{aligned}
\qquad (3.7)
$$

Infrared light couples with the electric dipole of the crystal $D_\alpha(t) = \sum_{ls\beta} Z_{\alpha\beta}(ls) u_\beta(ls; t)$, where $Z_{\alpha\beta}(ls)$ is the Born effective charge tensor of atom s at site l, $u_\beta(ls; t)$ is the β component of the displacement at time t. With the interaction Hamiltonian $\mathbf{H_I}(t) = -\mathbf{D} \cdot \mathbf{E} e^{-i\omega t}$, the dielectric susceptibility $\chi_{\alpha\beta}$ can be derived from $\frac{\delta \langle D_\alpha \rangle}{E_\beta}$ as

$$
\begin{aligned}
\chi_{\alpha\beta}(\omega) &= -\frac{1}{NV_c} \int_{-\infty}^{+\infty} \frac{\theta(t - t')}{i\hbar} \langle [D_\alpha(t), D_\beta(t')] \rangle e^{i\omega(t - t')} d(t - t') \\
&= -\frac{1}{NV_c} \sum_{ls\gamma} \sum_{l's'\delta} Z_{\alpha\gamma}(ls) Z_{\beta\delta}(l's') G_{\gamma\delta}(ls, l's'; \omega)
\end{aligned}
\qquad (3.8)
$$

44

where V_c is the volume of a single cell and N is the number of the cells in the whole crystal. $G_{\alpha\beta}(ls, l's'; \omega)$ is the Fourier transform of the one-phonon Green's function $G_{\alpha\beta}(ls, l's'; t - t')$, defined as:

$$G_{\alpha\beta}(ls, l's'; t - t') = \frac{\theta(t - t')}{i\hbar} \langle [u_\alpha(ls; t), u_\beta(l's'; t')].\rangle \tag{3.9}$$

3.3 One-phonon Green's Function

From the previous section we know that computing the dielectric susceptibility is equivalent to evaluating the one-phonon Green's function $G_{\alpha\beta}(ls, l's'; t - t')$. A. A. Maradudin and A. E. Fein [58] explicitly calculated this Green's function for pure crystals with anharmonicity. R. J. Elliott et $al.$[59] summarized the techniques for disordered crystals. Here I present a simple extension suitable for the cases where both anharmonicity and disorder scattering are important. This extension is the basis of our treatment for the infrared properties of ferropericlase.

The vibrational Hamiltonian for a crystal in general, up to the third order anharmonic interaction, can be written as:

$$\begin{aligned}
H &= \sum_{ls\alpha} \frac{p_\alpha^2(ls)}{2M(ls)} + \frac{1}{2} \sum_{l_1 s_1 \alpha} \sum_{l_2 s_2 \beta} \Phi_{\alpha\beta}(l_1 s_1, l_2 s_2) u_\alpha(l_1 s_1) u_\beta(l_2 s_2) \\
&+ \frac{1}{3!} \sum_{l_1 s_1 \alpha} \sum_{l_2 s_2 \beta} \sum_{l_3 s_3 \gamma} \Phi_{\alpha\beta\gamma}(l_1 s_1, l_2 s_2, l_3 s_3) u_\alpha(l_1 s_1) u_\beta(l_2 s_2) u_\gamma(l_3 s_3) \quad (3.10)
\end{aligned}$$

Where $p_\alpha(ls)$ denotes the α cartesian component of the momentum of the sth atom in the lth unit cell, $M(ls)$ is the mass of that atom, $u_\alpha(ls)$ is its displacement. $\Phi_{\alpha\beta}(l_1 s_1, l_2 s_2)$, $\Phi_{\alpha\beta\gamma}(l_1 s_1, l_2 s_2, l_3 s_3)$ are the atomic force constants of the second, third

order, respectively.

From the commutation relations for the $\{u_\alpha(ls)\}$ and $\{p_\alpha(ls)\}$:

$$[u_\alpha(ls), u_\beta(l's')] = [p_\alpha(ls), p_\beta(l's')] = 0$$

$$[u_\alpha(ls), p_\beta(l's')] = i\hbar\delta_{ll'}\delta_{ss'}\delta_{\alpha\beta} \qquad (3.11)$$

we know:

$$\dot{u}_\alpha(ls) = \frac{1}{i\hbar}[u_\alpha(ls), H] = \frac{p_\alpha(ls)}{M(ls)}$$

$$\ddot{u}_\alpha(ls) = \frac{1}{i\hbar}[\dot{u}_\alpha(ls), H]$$

$$= -\frac{1}{M(ls)}(\sum_{l_1 s_1 \beta} \Phi_{\alpha\beta}(ls, l_1 s_1)u_\beta(l_1 s_1)$$

$$+\frac{1}{2}\sum_{l_1 s_1 \beta}\sum_{l_2 s_2 \gamma} \Phi_{\alpha\beta\gamma}(ls, l_1 s_1, l_2 s_2)u_\beta(l_1 s_1)u_\gamma(l_2 s_2))$$

$$(3.12)$$

The real-time retarded Green's function $G_{\alpha\beta}(ls, l's'; t - t')$ satisfies

$$\dot{G}_{\alpha\beta}(ls, l's'; t) = \frac{\theta(t)}{i\hbar M(ls)}\langle[p_\alpha(ls; t), u_\beta(l's'; 0)]\rangle$$

$$\ddot{G}_{\alpha\beta}(ls, l's'; t) = -\frac{\delta(t)\delta_{ll'}\delta_{ss'}\delta_{\alpha\beta}}{M(ls)} - \frac{1}{M(ls)}(\sum_{l_1 s_1 \gamma} \Phi_{\alpha\gamma}(ls, l_1 s_1)\frac{\theta(t)}{i\hbar}\langle[u_\gamma(l_1 s_1; t), u_\beta(l's'; 0)]\rangle$$

$$+\frac{1}{2}\sum_{l_1 s_1 \gamma}\sum_{l_2 s_2 \delta} \Phi_{\alpha\gamma\delta}(ls, l_1 s_1, l_2 s_2)\frac{\theta(t)}{i\hbar}\langle[u_\gamma(l_1 s_1; t)u_\delta(l_2 s_2; t), u_\beta(l's'; 0)]\rangle)$$

$$= -\frac{\delta(t)\delta_{ll'}\delta_{ss'}\delta_{\alpha\beta}}{M(ls)} - \frac{1}{M(ls)}(\sum_{l_1 s_1 \gamma} \Phi_{\alpha\gamma}(ls, l_1 s_1)G_{\gamma\beta}(ls, l_1 s_1; t)$$

$$+\frac{1}{2}\sum_{l_1 s_1 \gamma}\sum_{l_2 s_2 \delta} \Phi_{\alpha\gamma\delta}(ls, l_1 s_1, l_2 s_2)G_{\gamma\delta,\beta}(l_1 s_1 l_2 s_2, l's'; t)) \qquad (3.13)$$

46

where

$$G_{\gamma\delta,\beta}(l_1 s_1 l_2 s_2, l's'; t - t')) = \frac{\theta(t - t')}{i\hbar} \langle [u_\gamma(l_1 s_1; t) u_\delta(l_2 s_2; t), u_\beta(l's'; t')] \rangle \quad (3.14)$$

For convenience, we define $g_{\alpha\beta}(ls, l's'; t)$ as the Green's function for an ideal perfect crystal, i.e., without disorder scattering and anharmonicity. $G^0_{\alpha\beta}(ls, l's'; t)$ is the Green's function for a disorder crystal without anharmonicity. Then as shown in Ref. [60], they will satisfy:

$$M(ls)\omega^2 G^0_{\alpha\beta}(ls, l's'; \omega) = \delta_{ll'}\delta_{ss'}\delta_{\alpha\beta} + \sum_{l_1 s_1 \gamma} \Phi_{\alpha\gamma}(ls, l_1 s_1) G^0_{\gamma\beta}(l_1 s_1, l's'; \omega) \quad (3.15)$$

Or in a more compact matrix form:

$$-\mathbf{M}\omega^2 \mathbf{G}^0(\omega) + \mathbf{\Phi}\mathbf{G}^0(\omega) + \mathbf{I} = 0$$

or

$$\mathbf{G}^0(\omega)^{-1} = \mathbf{M}\omega^2 - \mathbf{\Phi} \quad (3.16)$$

On the other hand, the Green's function $\mathbf{g}$ for perfect crystal will satisfies:

$$\mathbf{g}(\omega)^{-1} = \mathbf{M}_0\omega^2 - \mathbf{\Phi}^0 \quad (3.17)$$

If we define a perturbation matrix

$$\mathbf{C}(\omega) = (\mathbf{M}_0 - \mathbf{M})\omega^2 + \mathbf{\Phi} - \mathbf{\Phi}^0 \quad (3.18)$$

we get Dyson equation relating $\mathbf{g}(\omega)$ and $\mathbf{G}^0(\omega)$

$$\mathbf{G}^0(\omega) = \mathbf{g}(\omega) + \mathbf{g}(\omega)\mathbf{C}\mathbf{G}^0(\omega) \tag{3.19}$$

To study anharmonicity from perturbation theory, we can either use the eigenvectors of the pure crystal as the basis set, denoted as $\frac{1}{\sqrt{N}}\hat{e}_\alpha(s|\mathbf{q}j)e^{i\mathbf{q}\cdot\mathbf{R}(ls)}$ or use those of the disordered crystal, denoted as $e_\alpha(s|j)$. In the eigenvector representation:

$$g_{\alpha\beta}(ls, l's'; \omega) = \sum_{\mathbf{q}j} \frac{\hat{e}_\alpha(s|\mathbf{q}j)\hat{e}_\beta^*(s'|\mathbf{q}j)e^{i\mathbf{q}\cdot(\mathbf{R}(ls)-\mathbf{R}(l's'))}}{N\sqrt{M(s)M(s')}(\omega^2 - \omega_{\mathbf{q}j}^2 + i2\omega\eta)}, \tag{3.20}$$

$$G_{\alpha\beta}^0(ls, l's'; \omega) = \sum_{j} \frac{e_\alpha(ls|j)e_\beta^*(l's'|j)}{\sqrt{M(ls)M(l's')}(\omega^2 - \omega_j^2 + i2\omega\eta)}, \tag{3.21}$$

The higher order Green's function in Eq. (3.14) can be calculated from its own equation of motion, then factorized to products of one-phonon Green's function $G_{\alpha\beta}(ls, l's'; t)$ approximately. To simplify notation, we abbreviate each coordinate $u_\alpha(ls; t)$ by its subscript $u_\alpha(t)$:

$$\ddot{G}_{\gamma\delta,\beta}(t - t') = -\sum_{\rho} \frac{\theta(t - t')}{i\hbar}\langle[u_\gamma(t)u_\delta(t), u_\rho(t')]\rangle\frac{\Phi_{\rho\beta}}{M_\beta}$$
$$-\sum_{\sigma}\sum_{\tau}\frac{\theta(t - t')}{i\hbar}\langle[u_\gamma(t)u_\delta(t), u_\sigma(t')u_\tau(t')]\rangle\frac{\Phi_{\sigma\tau\beta}}{2M_\beta}\rangle \tag{3.22}$$

Do the Fourier transform:

$$G_{\gamma\delta,\beta}(\omega) = \frac{1}{2}G_{\gamma\delta,\sigma\tau}(\omega)\Phi_{\sigma\tau\rho}G_{\rho\beta}^0(\omega) \tag{3.23}$$

where $G_{\gamma\delta,\sigma\tau}(\omega)$ is the Fourier transform of the two-phonon Green's function:

$$G_{\gamma\delta,\sigma\tau}(t - t') = \frac{\theta(t - t')}{i\hbar}\langle[u_\gamma(t)u_\delta(t), u_\sigma(t')u_\tau(t')]\rangle \tag{3.24}$$

Thus the full equation of motion can be written as:

$$
\begin{aligned}
G_{\alpha\beta}(\omega) &= g_{\alpha\beta}(\omega) + g_{\alpha\gamma}(\omega)C_{\gamma\delta}G_{\delta\beta}(\omega) + \frac{1}{4}g_{\alpha\lambda}\Phi_{\lambda\gamma\delta}G_{\gamma\delta,\sigma\tau}(\omega)\Phi_{\sigma\tau\rho}G^0_{\rho\beta}(\omega) \\
&= g_{\alpha\beta}(\omega) + g_{\alpha\lambda}(\omega)(C_{\lambda\rho} + \frac{1}{4}\Phi_{\lambda\gamma\delta}G_{\gamma\delta,\sigma\tau}(\omega)\Phi_{\sigma\tau\rho})G_{\rho\beta}(\omega) \tag{3.25}
\end{aligned}
$$

The last factor $G^0_{\rho\beta}(\omega)$ is replaced by $G_{\rho\beta}(\omega)$ when we only consider irreducible diagrams. In the next chapter we compute the contribution from disorder $C_{\lambda\rho}$ and anharmonicity $\frac{1}{4}\Phi_{\lambda\gamma\delta}G_{\gamma\delta,\sigma\tau}(\omega)\Phi_{\sigma\tau\rho}$ separately.

The two-phonon Green's function appearing in Eq. (3.25), $G_{\gamma\delta,\sigma\tau}(\omega)$, can be approximated as product of two one-phonon Green's functions: $G_{\gamma\delta,\sigma\tau} = G_{\gamma\delta}G_{\sigma\tau} + G_{\gamma\tau}G_{\sigma\delta}$. The one-phonon Green's functions can further be approximated by non-interacting Green's function $\mathbf{g}$. Then we get a self-energy diagram as shown in Fig. 3.1. The evaluation of this diagram is standard and can be found in [50, 58].

3.4   Shell Model

Shell Model was proposed by Dick and Overhauser [61] in 1958. It is the standard empirical model to describe the vibrational properties of insulators. In the shell model, each ion consists of a massive core and massless shell, which are connected by a spring. The spring mimics the electronic polarization accompanied with the ionic movement. The electron shell is massless in accordance with the Born-Oppenheimer
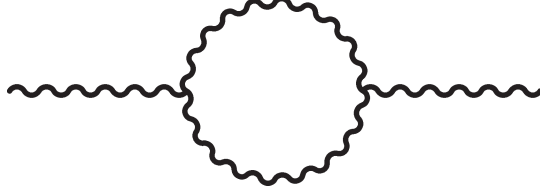
Figure 3.1: Ring diagram of phonon-phonon interaction due to the third order anharmonic potential.

approximation. The core and shell are charged and have Coulomb interactions. There are empirical repulsive potentials between the shells of different ions, to balance the Coulomb attraction. Such empirical potentials can be taken as Lennard-Jones form or Buckingham form:

$$
\begin{aligned}
U_{ij}^{\text{Lennard}-\text{Jones}} &= \frac{C_m}{r_{ij}^m} - \frac{C_6}{r_{ij}^6} \\
U_{ij}^{\text{Buckingham}} &= A \exp\left(-\frac{r_{ij}}{\rho}\right) - \frac{C_6}{r_{ij}^6}
\end{aligned}
\tag{3.26}
$$

The shell model obeys the equation of motion,

$$
\begin{cases}
\mathbf{M}_c \ddot{\mathbf{u}}_c = \mathbf{D}_{cc}\mathbf{u}_c + \mathbf{D}_{cs}\mathbf{u}_s \\
0 = \mathbf{D}_{sc}\mathbf{u}_c + \mathbf{D}_{ss}\mathbf{u}_s
\end{cases}
\tag{3.27}
$$

or

$$
-\omega^2 \mathbf{M}_c \mathbf{u}_c = (\mathbf{D}_{cc} - \mathbf{D}_{cs}\mathbf{D}_{ss}^{-1}\mathbf{D}_{sc})\mathbf{u}_c
\tag{3.28}
$$
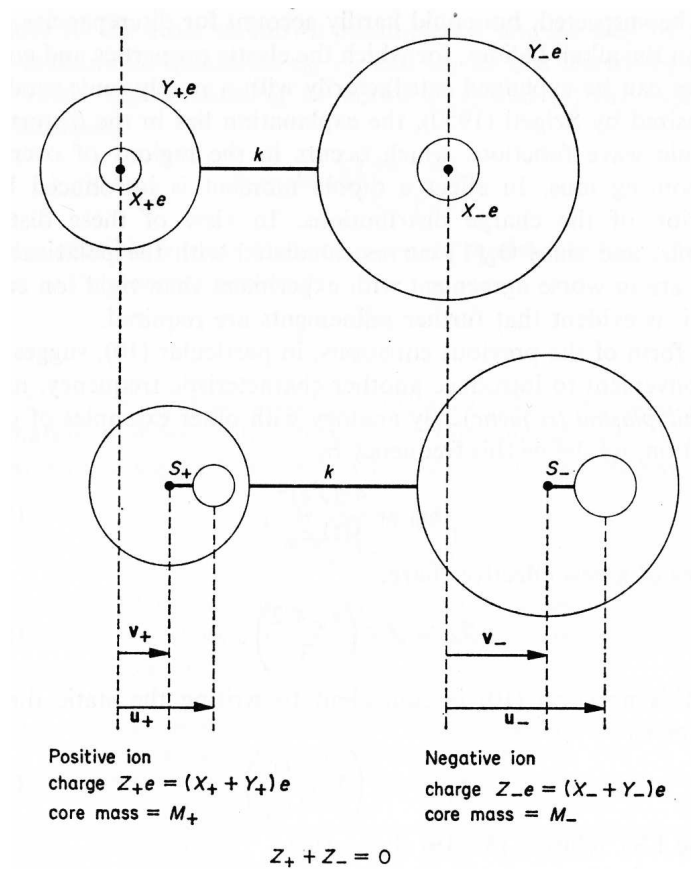
Figure 3.2: Illustration of the Shell model. (Taken from Ref. [63])

where $\mathbf{D}_{cc}$, $\mathbf{D}_{cs}$, $\mathbf{D}_{sc}$ and $\mathbf{D}_{ss}$ denote the force matrix between core-core, core-shell, shell-core and shell-shell interactions respectively. While $\mathbf{u}_c$ and $\mathbf{u}_s$ are the displacements of the core and shell. $\mathbf{M}_c$ is the mass matrix of the core. After solving the equation of motion, we can obtain all the other vibrational properties, which are functions of $\mathbf{u}_c$ and $\mathbf{u}_s$. Further details can be found in Ref. [62].

Chapter 4

Infrared Properties of Ferropericlase ($Mg_{1-x}Fe_xO$): Experiment and Theory

4.1   Introduction

Ferropericlase, ($Mg_{1-x}Fe_xO$, with $x = 0.10 - 0.15$), is thought to be one of the major constituents of the earth's lower mantle ($660 - 2900$ km depth).[64] The name 'magnesiowüstite' is also used, but properly refers to the doping region x close to the wüstite (x=1), rather than the periclase (x=0) limit. In contrast with periclase (pure MgO), which is a typical ionic insulator with a band gap of 7.8 eV,[65] ferropericlase has crystal field levels and charge transfer bands at much lower energies due to the presence of Fe^{2+}. These electronic excitations have been studied by measuring the optical absorption spectra in the frequency range of about 2000 to $25,000$ cm^{-1}.[66, 67] The presence of Fe^{2+} also influences the vibrational excitations of the system. With

strong disorder scattering of propagating vibrational states, the harmonic eigenstates of the disordered crystal do not necessarily have a well defined wave number, and may not propagate ballistically. One way to study the vibrational excitations is by doing infrared (IR) reflectance spectroscopy. To our knowledge, such a study for $Mg_{1-x}Fe_xO$, with $x < 0.4$, has not been carried out yet.

In pure MgO, the anharmonic phonon-phonon interactions causes a shoulder at ~ 640 cm^{-1} in the IR reflectance spectrum.[68] Thus anharmonicity should also be included in analyzing the infrared reflectance of ferropericlase.

In this paper we report the temperature-dependent infrared reflectance measurements of magnesium oxide and ferropericlase for several Fe concentrations at ambient pressure. We construct a model in which anharmonic phonon-phonon interactions and disorder scattering are treated separately. Their effects are then combined for comparison with the experimental data.

4.2   Experimental Measurements

Our samples are homogeneously-doped single crystals, in which $Fe^{3+}/\sum Fe \approx 0.02$ for the 6% sample and 0.05 for the 27% sample. In our analysis, the influence of Fe^{3+} and magnesium vacancies is ignored. A detailed description of the samples' synthesis, crystallography and elastic properties is in Ref. [69]. The samples are rectangular slabs with typical dimensions of $1\,\mathrm{mm} \times 2\,\mathrm{mm}$, with a thickness of ≈ 0.3 mm. In order to reduce interference effects due to reflections from the back surface, the samples have been wedged. However, due to the thin nature of the samples, the largest wedge that could be introduced was $\simeq 15°$. The reflectance spectra has been measured at a near-normal angle of incidence at 295 and 6 K over a wide frequency range from

≈ 50 to about $32\,000$ cm^{-1} on Bruker IFS 66v/S and 113v spectrometers using an *in-situ* evaporation technique.[70] Figure 4.1(a) shows the measured reflectance at 6 K in the whole frequency range. Figure 4.1(b), (c) and (d) show the measured reflectance at 295 and 6 K of pure MgO, and $Mg_{1-x}Fe_xO$, for $x = 0.06$ and $x = 0.27$ respectively. Although wedging the samples has been very effective at reducing interference effects, weak fringes may still be detected at low temperature below about 150 cm^{-1}. The complex dielectric function $\epsilon = \epsilon_1 + i\epsilon_2$ has been determined from a Kramers-Kronig analysis of the reflectance, where extrapolations are supplied for $\omega \to 0, \infty$. At low frequency, an insulating response is assumed and $R(\omega \to 0) \simeq 0.27$, 0.28 and 0.31 for MgO, and the 6% and 27% Fe-doped materials, respectively. Above the highest measured frequency the reflectance has been assumed to be constant to approximately $75\,000$ cm^{-1}, above which a free-electron approximation has been assumed $(R \propto 1/\omega^4)$. The imaginary part of the resulting dielectric functions at 6 and 295 K of pure MgO, and $Mg_{1-x}Fe_xO$, for $x = 0.06$ and $x = 0.27$, are shown in Figs. 4.1(e), (f) and (g), respectively. They contain most of the physical information, and are the focus of our theoretical analysis. The optical features have been fit to a classical oscillator model using the complex dielectric function

$$\epsilon(\omega) = \epsilon_\infty + \sum_j \frac{\omega_{p,j}^2}{\omega_{\text{TO},j}^2 - \omega^2 - i2\omega\gamma_j}, \tag{4.1}$$

where ϵ_∞ is a high-frequency contribution, and $\omega_{\text{TO},j}$, $2\gamma_j$ and $\omega_{p,j}$ are the frequency, full width and strength of the jth vibration. The results of non-linear least-squares fits to the reflectance and $\epsilon_2(\omega)$ are shown in Table 4.1. In addition to the strong feature in $\epsilon_2(\omega)$ seen at about 400 cm^{-1}, other features at ≈ 520 and ≈ 640 cm^{-1} are also clearly visible in $\epsilon_2(\omega)$ shown in Fig. 4.1; however, these features are very weak

Table 4.1: A comparison of the fitted values of the static and high-frequency contributions to the real part of the dielectric function at room temperature, as well as the fitted frequency, full width and strength (ω_{TO}, 2γ and ω_p, respectively) of the feature associated with the strong TO mode in MgO, and the 6% and 27% Fe-doped materials at 295 and 6 K. The units of ω_{TO}, 2γ and ω_p are in cm^{-1}. The strength of the TO mode is also expressed as a dimensionless oscillator strength $S = \omega_p^2/\omega_{\text{TO}}^2$. Values of ϵ_0 and ϵ_∞ are at 295 K, the estimated uncertainty is about ± 0.1. The uncertainty in ω_{TO} is ± 0.1 cm^{-1}. The uncertainties for 2γ are ± 0.1 cm^{-1} in the pure material, and ± 0.5 cm^{-1} in the Fe-doped materials. The uncertainty in ω_p is ± 20 cm^{-1}.

				295 K		6 K		
Mg$_{1-x}$Fe$_x$O	ϵ_0	ϵ_∞	ω_{TO}	2γ	ω_p (S)	ω_{TO}	2γ	ω_p (S)
pure	9.2	2.95	396.5	3.44	1010 (6.5)	398.9	1.72	1030 (6.7)
$x = 0.06$	10.8	3.10	395.6	30.5	1090 (7.6)	396.7	29.1	1120 (8.0)
$x = 0.27$	11.8	3.65	384.5	28.6	1100 (8.2)	388.6	25.7	1140 (8.6)

and as a result the strengths and widths of these modes are difficult to determine reliably.

4.3 Computational Methods

4.3.1 General Scheme

Infrared dielectric properties of ionic crystals are contained in the linear response function $\epsilon_{\alpha\beta}(\omega) = \epsilon_{\alpha\beta}(\infty) + 4\pi\chi_{\alpha\beta}(\omega)$.[50] Considering only the first-order moment of the electric dipole, the dielectric susceptibility of a crystal can be related to its displacement-displacement retarded Green's function by:

$$\chi_{\alpha\beta}(\omega) = -\frac{1}{NV_c} \sum_{ls\gamma} \sum_{l's'\delta} Z_{\alpha\gamma}(ls) Z_{\beta\delta}(l's') G_{\gamma\delta}(ls, l's'; \omega), \qquad (4.2)$$

where $Z_{\alpha\beta}(ls)$ is the Born effective charge tensor of the atom s at site l. The volume of a single cell is V_c, and N is the number of the cells in the whole crystal. The
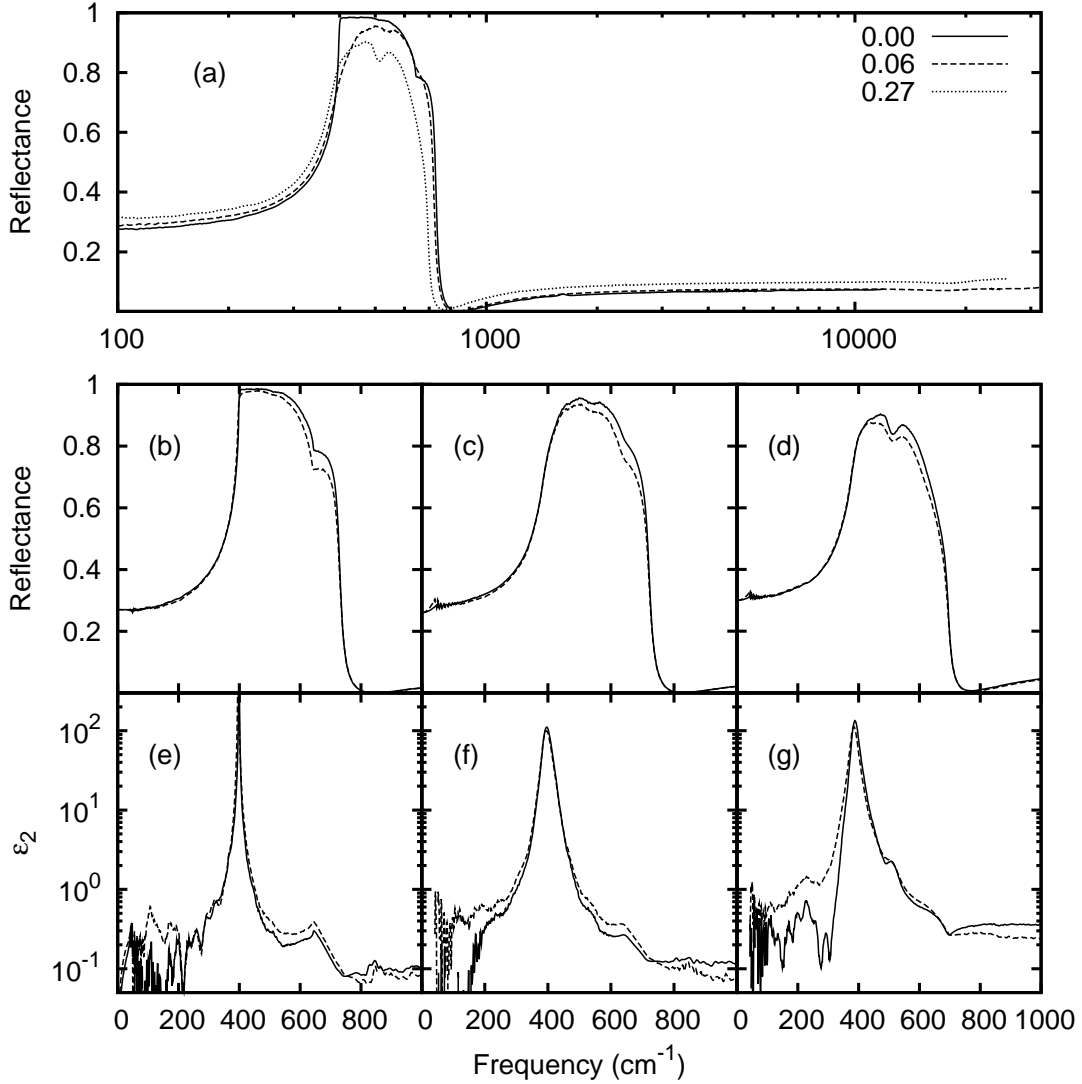
Figure 4.1: The measured reflectance $r(\omega)$; (a) in the whole frequency range at 6 K. Parts below 1000 cm^{-1} are shown in: (b) pure MgO, and Mg$_{1-x}$Fe$_x$O for (c) 6% and (d) 27% Fe-doping. The corresponding imaginary part of the dielectric functions $\epsilon_2(\omega)$; (e) pure MgO, and Mg$_{1-x}$Fe$_x$O for (f) 6% and (g) 27% Fe-doping. The solid line corresponds to data measured at 6 K, dashed line corresponds to data at 295 K.

Green's function $G_{\alpha\beta}(ls, l's'; \omega)$ can be evaluated from its equation of motion.[60] For a harmonic material, the vibrational Hamiltonian is quadratic and can be solved exactly. We denote the eigenvectors of a pure crystal as $\frac{1}{\sqrt{N}}\hat{e}_\alpha(s|\mathbf{q}j)e^{i\mathbf{q}\cdot\mathbf{R}(ls)}$, the corresponding eigenvalues as $\omega_{\mathbf{q}j}$, those of a disordered crystal as $e_\alpha(s|j)$ and ω_j, the Green's function of the pure as $\mathbf{g}$, the disordered as $\mathbf{G}^0$. Then

$$g_{\alpha\beta}(ls, l's'; \omega) = \sum_{\mathbf{q}j} \frac{\hat{e}_\alpha(s|\mathbf{q}j)\hat{e}_\beta^*(s'|\mathbf{q}j)e^{i\mathbf{q}\cdot(\mathbf{R}(ls)-\mathbf{R}(l's'))}}{N\sqrt{M(s)M(s')}(\omega^2 - \omega_{\mathbf{q}j}^2 + i2\omega\eta)}, \qquad (4.3)$$

$$G_{\alpha\beta}^0(ls, l's'; \omega) = \sum_j \frac{e_\alpha(ls|j)e_\beta^*(l's'|j)}{\sqrt{M(ls)M(l's')}(\omega^2 - \omega_j^2 + i2\omega\eta)}, \qquad (4.4)$$

where the mass of the atom s is denoted as $M(s)$ in the pure crystal, $M(ls)$ in the disordered crystal, with the extra label l to specify its site, η is an infinitesimal number ensuring causality.

Anharmonic interaction will couple these modes and make exact solution impossible. The standard treatment of this many-body effect uses the Dyson equation to define a self-energy for each mode. We can either choose $e_\alpha(s|j)$ as the unperturbed states, then the only interaction will be anharmonicity, or choose $\frac{1}{\sqrt{N}}\hat{e}_\alpha(s|\mathbf{q}j)e^{i\mathbf{q}\cdot\mathbf{R}(ls)}$ as the basis and treat disorder as an extra perturbation. The first approach has been used by one of the authors to study the anharmonic decay of vibrational states in amorphous silicon. [71] In this paper we use a hybrid approach. We write the dielectric function of a disordered anharmonic crystal in the perfect crystal harmonic basis as

$$\epsilon_{\alpha\beta}(\omega) = \epsilon_{\alpha\beta}(\infty) + \frac{4\pi}{V_c}\sum_{j=1}^{\mathrm{TO}} \frac{\sum_{s\gamma} Z_{\alpha\gamma}(s)\frac{\hat{e}_\gamma(s|0j)}{\sqrt{M(s)}}\sum_{s'\delta} Z_{\beta\delta}(s')\frac{\hat{e}_\delta^*(s'|0j)}{\sqrt{M(s')}}}{\{\omega(0j)^2 - \omega^2 + 2\omega(0j)(\Delta(0j,\omega) - i\Gamma(0j,\omega))\}}, (4.5)$$

where $\omega(0j) \equiv \omega_{\mathrm{TO},j}$ is the frequency at $\mathbf{q} = 0$ of the jth TO branch. The terms $\Delta(0j, \omega)$ and $\Gamma(0j, \omega)$ correspond to the real and imaginary part of the mode's self-energy $\Sigma(0j, \omega)$. Then we split this self-energy into two parts: $\Sigma = \Sigma_{\mathrm{anharm}} + \Sigma_{\mathrm{disorder}}$. Each piece is calculated independently. This is equivalent to omitting all the diagrams where the disorder scattering vertex appears inside an anharmonic interaction loop. The anharmonic interaction of ferropericlase is assumed to be the same as that of pure MgO, i.e. the influence of disorder on anharmonic coefficients is totally ignored. Disorder is treated by exact diagonalization without anharmonicity, it is then converted to a self-energy of the TO mode in the perfect crystal harmonic basis. These approximations are tested by comparing with the experimental results.

4.3.2 Shell Model

The scheme described above is general. It does not depend on which microscopic model is chosen to get harmonic phonons, disorder scattering strength, and higher-order force constants. Here we use an anharmonic shell model, with shell parameters fitted to experiments. The harmonic phonon properties in this paper are calculated with the general utility lattice program (GULP) code.[72]

Two sets of shell parameters[72, 73] are used for MgO: S-I and B, and one for FeO: S-II. S-I and S-II are rigid shell models in which O^{2-} has the same set of parameters, thus they can be conveniently used to simulate ferropericlase. B is an isotropic breathing shell model which gives better fit to the experimental data. However, it can not be directly used for ferropericlase. For FeO the elastic constants $C_{12} > C_{44}$, while the isotropic breathing shell model is only suitable for cases where $C_{12} < C_{44}$.[74] We treat B as a reference to check our anharmonic calculations based on S-I. All the

Table 4.2: Shell model parameters used in the calculation. They are taken from Refs. [72, 73]. The short-range repulsive potential is assumed to be a two-body Buckingham type: for S-I and S-II, $V(r) = A\exp(-r/\rho) - C/r^6$; for B, $V(r) = A\exp(-(r-r_0)/\rho) - C/r^6$. The parameter k represents the spring constant between core and shell. Rows in which atomic symbols have a star (*) are for the B model. The label 'shell' denotes a potential that acts on the central position of the shell, while 'bshell' denotes an interaction that acts on the radius of the shell which was fixed at 1.2 Å. An extra parameter in B model is $k_{\mathrm{BSM}} = 351.439$ eV·Å^{-2}. The equilibrium shell radius r_0 is 1.1315 Å after optimization.

	Z_{core} (e)	Z_{shell} (e)	k (eV)
O	0.9345	−2.9345	51.712
Mg	2	−	−
Fe	−1.1682	3.1682	69.562
O*	0.8	−2.8	46.1524
Mg*	2	−	−
	A (eV)	ρ (Å)	C (eV·Å^6)
O shell-O shell	22764.3	0.149	20.37
Mg core-O shell	1346.6	0.2984	0.0
Fe shell-O shell	1231.2	0.3086	0.0
O* shell-O* shell	0.0	0.3	54.038
Mg* core-O* bshell	28.7374	0.3092	0.0

model parameters are listed in Table 4.2. Table 4.3.2 contains the calculated physical properties and corresponding experimental values. Phonon dispersion curves for the pure crystals of MgO and FeO are shown in Fig. 4.2.

4.3.3 Anharmonicity

A complete calculation of anharmonicity is tedious, even for a pure crystal.[50] Thus we ignore the less important terms and focus on the dominant one. From Eq. (4.5) it is clear that since $|\Sigma| = |\Delta - i\Gamma|$ is small compared to ω_{TO}, the real part of the self-energy Δ has negligible influence on $\epsilon_2(\omega)$, except to shift its resonant frequency. The shell
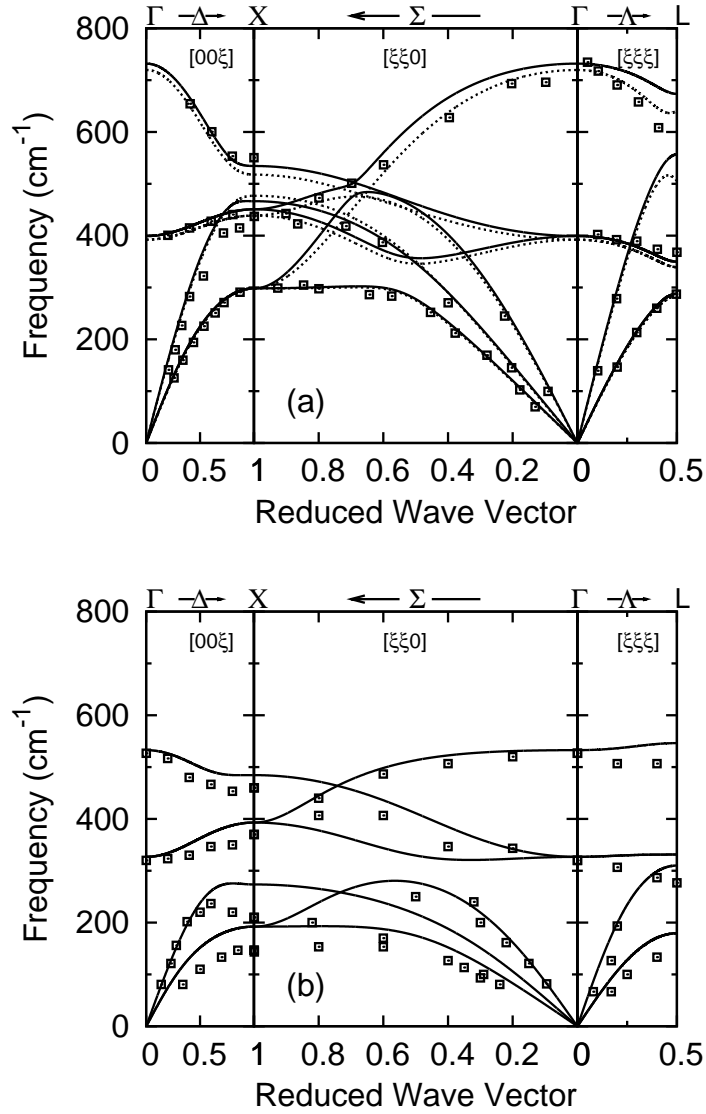
Figure 4.2: Phonon dispersions of the pure crystals. (a) MgO, solid line corresponds to the rigid-shell model S-I, dashed line to the isotropic breathing-shell model B, dots are the experimental data taken from Ref. [75]; (b) FeO, solid line corresponds to the rigid-shell model S-II, dots are the experimental data taken from Ref. [76].

Table 4.3: Physical properties of pure MgO and FeO, compared with shell model results.

	a (Å)	C_{11} (GPa)	C_{12} (GPa)	C_{44} (GPa)	ϵ_0	ϵ_∞	TO (cm^{-1})
MgO (exp[a])	4.212	297.0	95.2	155.7	9.86	2.96	401
S-I	4.225	370.9	163.0	163.0	9.88	2.94	399
B	4.212	297.0	95.0	155.7	9.89	2.94	392
FeO (exp[b])	4.310	359	156	56	14.2	5.4	320
S-II	4.324	327	149	149	14.18	5.34	327

[a]References [72, 73, 77].
[b]Reference [77]

models we use are fitted to the experimental data measured at room temperature. The anharmonic shift is small, compared with the shift caused by impurity scattering. Thus, we ignore it completely and only consider the imaginary part of the self energy $\Gamma_{\text{anharm}}(0j, \omega)$. To the lowest order $\Gamma_{\text{anharm}}(0j, \omega)$ can be written as[50]

$$
\Gamma_{\text{anharm}}(0j, \omega) = \frac{18\pi}{\hbar^2} \sum_{\mathbf{q}j_1j_2} \left| V \begin{pmatrix} 0 & \mathbf{q} & -\mathbf{q} \\ j & j_1 & j_2 \end{pmatrix} \right|^2 \{(n_1 + n_2 + 1)[\delta(\omega_1 + \omega_2 - \omega) - \quad (4.6)
$$
$$
\delta(\omega_1 + \omega_2 + \omega)] + (n_2 - n_1)[\delta(\omega_2 - \omega_1 + \omega) - \delta(\omega_1 - \omega_2 + \omega)]\},
$$

where $n_1 = n(\mathbf{q}j_1)$ is the Bose-Einsein population factor of the mode, and $\omega_1 = \omega(\mathbf{q}j_1)$ is the corresponding frequency. The anharmonic coefficient $V \begin{pmatrix} 0 & \mathbf{q} & -\mathbf{q} \\ j & j_1 & j_2 \end{pmatrix}$ is computed from the nearest neighbor third-order force constants $\Phi_{\alpha\beta\gamma} \begin{pmatrix} 0 & l_2 & l_3 \\ s_1 & s_2 & s_3 \end{pmatrix}$ using standard formulas.[50, 78, 79] Other parameters (Born effective charge tensors, harmonic eigenvectors) are obtained from GULP. The integration over q-space is done with the tetrahedron method, using 1/48 of the Brillouin zone, and averaging over x, y, and z polarizations. We use 3345 q-points, equivalent to 160560 q-points in the whole Brillouin zone.

4.3.4 Disorder Scattering

The self-energy of a vibrational mode caused by disorder scattering is defined statistically, [59, 60]

$$\langle\!\langle \mathbf{G^0} \rangle\!\rangle = \mathbf{g} + \mathbf{g}\mathbf{\Sigma}\langle\!\langle \mathbf{G^0} \rangle\!\rangle,$$

where $\langle\!\langle \mathbf{G^0} \rangle\!\rangle$ denotes the Green's function averaged over different impurity distributions. We slightly modify this definition by including the Born effective charge. From Eqs. (4.3) and (4.4), we define the following equation

$$\langle\!\langle \sum_\gamma \sum_\delta Z_{\alpha\gamma}(ls)G^0_{\gamma\delta}(ls,l's';\omega)Z_{\delta\beta}(l's') \rangle\!\rangle = \sum_\gamma \sum_\delta Z_{\alpha\gamma}(s)\tilde{g}_{\gamma\delta}(ls,l's';\omega)Z_{\delta\beta}(s'), \tag{4.7}$$

where

$$\tilde{g}_{\gamma\delta}(ls,l's';\omega) = \sum_{\mathbf{q}j} \frac{\hat{e}_\gamma(s|\mathbf{q}j)\hat{e}^*_\delta(s'|\mathbf{q}j)e^{i\mathbf{q}\cdot(\mathbf{R}(ls)-\mathbf{R}(l's'))}}{N\sqrt{M(s)M(s')}(\omega^2 - \omega^2_{\mathbf{q}j} + i2\omega_{\mathbf{q}j}\Sigma_{\text{disorder}}(\mathbf{q}j,\omega))}. \tag{4.8}$$

The self-energy defined in this way guarantees that the dielectric susceptibilities calculated from $\mathbf{G}^0$ and $\tilde{\mathbf{g}}$ are the same. Summing over all sites of the crystal leaves only TO modes on the right hand side of Eq. (4.7). Thus, once we get the averaged dielectric susceptibility $\langle\!\langle \chi_{\alpha\beta} \rangle\!\rangle$ from the exact eigenvectors of the disordered crystal, we can extract the self-energy of its TO phonon.

We expand an orthogonal 8-atom MgO unit cell in each direction by 5 times, which gives a $5 \times 5 \times 5$ super-cell containing 1000 atoms. Then we randomly replace the corresponding number of Mg^{2+} by Fe^{2+}. The shell parameters of Mg^{2+} are from S-I model, those of Fe^{2+} are from S-II model, those of O^{2-} are the same in both models.

From Eqs. (4.2) and (4.4), for each configuration we have a harmonic susceptibility

$$\chi_{\alpha\beta}(\omega) = \frac{1}{NV_c} \sum_{j=1}^{modes} \frac{\displaystyle\sum_{ls\gamma} Z_{\alpha\gamma}(ls)\frac{e_\gamma(ls|j)}{\sqrt{M(ls)}} \sum_{l's'\delta} Z_{\beta\delta}(l's')\frac{e_\delta^*(l's'|j)}{\sqrt{M(l's')}}}{\omega_j^2 - \omega^2 - i2\omega\eta}. \tag{4.9}$$

We can choose a small value for η and evaluate Eq. (4.9) directly (Lorentzian broadening). However, insofar as η is finite, it is equivalent to have each mode j in Eq. (4.9) an imaginary self-energy (life time) linear in frequency ω. The self-energy of the TO phonon Σ_{disorder} extracted from this approach will depend on frequency linearly. Replacing the factor 2ω by $2\omega_j$ won't help either, as each mode j now has a life time independent of frequency, and Σ_{disorder} will be a constant depending on η when $\omega \to 0$. To avoid such artifacts we use

$$\frac{1}{\omega_j^2 - \omega^2 - i2\omega\eta} = \frac{1}{\omega_j^2 - \omega^2} + \frac{i\pi}{2\omega}\left[\delta(\omega - \omega_j) + \delta(\omega + \omega_j)\right]$$

to separate the real (χ_1) and imaginary part (χ_2) of the dielectric susceptibility. Then we divide the vibrational spectrum into equally sized bins (1 cm^{-1}) and compute χ_2 as a histogram. The real part χ_1 is obtained from χ_2 from the Kramers-Kronig relation. Many such super-cells are built and their ϵ_∞ and χ calculated. We find that 10 configurations are sufficient to give a well converged average. The final ϵ_∞ and χ are assumed to be the averaged values of all configurations. To remove the unphysical spikes caused by the finite size of our super-cells, while keeping the main features unchanged, we further smooth the dielectric susceptibility by averaging over adjacent

bins iteratively,

$$\chi_2^{n+1}(j) = \frac{1}{6} \left[\chi_2^n(j-1) + 4\chi_2^n(j) + \chi_2^n(j+1) \right].$$ (4.10)

In this way we successfully simulate the dielectric function of a 'real' crystal (real in the sense that except for finite size, disorder scattering is treated without any further approximations). These results, together with anharmonicity, are summarized in the next section.

4.4 Comparisons and Discussion

The anharmonic effects in pure MgO are shown in Fig. 4.3. The computational results and experimental values are quite close, especially near 640 cm^{-1} which corresponds to TO+TA combination mode. Below 800 cm^{-1}, the rigid shell model S-I and breathing shell model B give almost identical self-energies. The discrepancy in the high-frequency range indicates that the dispersion relations from empirical models are less accurate for high-frequency optical branches. The width of TO mode at the reststrahlen frequency ω_{TO} is less accurate, as $\Gamma_{\text{anharm}}(0j,\omega)$ is small in the region $\omega \approx \omega_{\text{TO}}$ and higher-order anharmonic effects become important.[80]

Figures 4.4 and 4.5 show how anharmonicity and disorder scattering influence the dielectric function. For the 6% sample it is clear that the shoulder near 640 cm^{-1} is caused by anharmonicity, while the shoulder at about 520 cm^{-1} is due to disorder scattering. Disorder scattering becomes stronger for the 27% sample and seems contributes to all the shoulders. The shoulder caused by anharmonicity corresponds to a peak in the two-phonon DOS, while shoulders caused by disorder scattering are
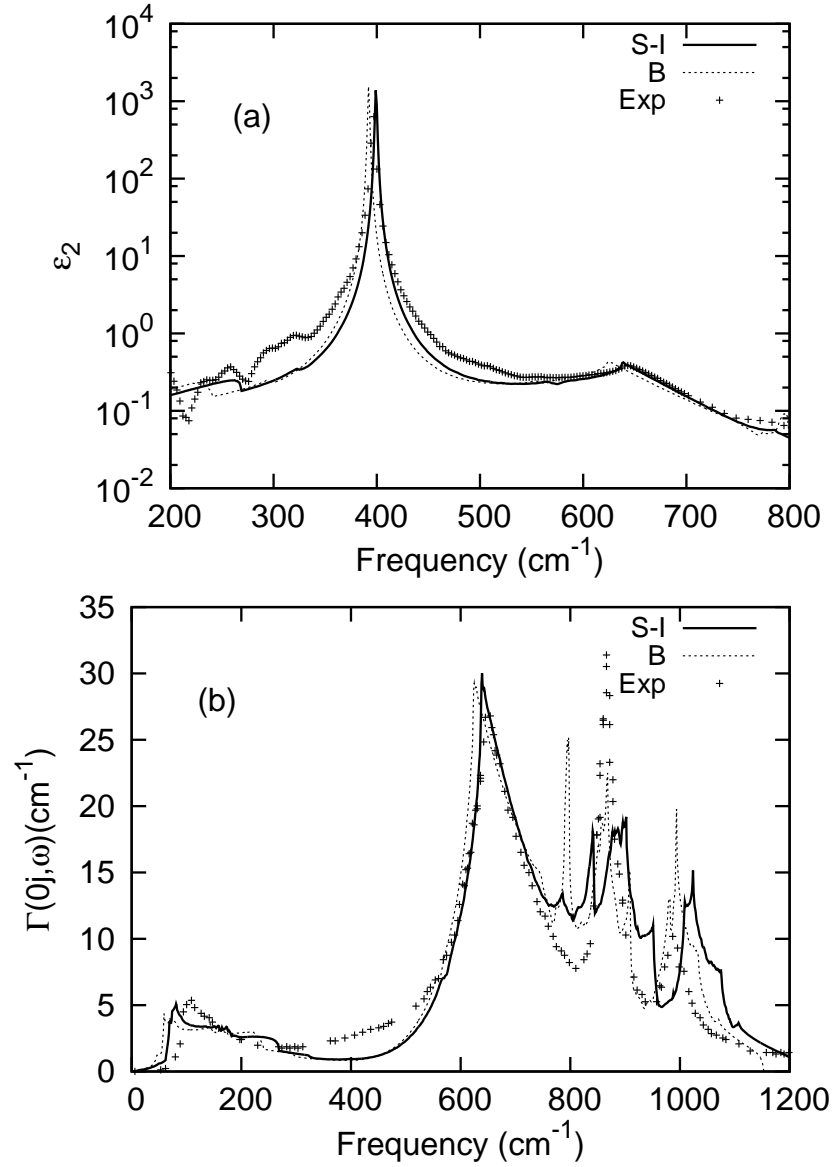
Figure 4.3: Computed anharmonic properties compared with experimental data for pure MgO. (a) The imaginary part of dielectric function at 295 K; the experimental data are the same as those in Fig. 4.1(d). (b) The imaginary part of self energy at 295 K; the experimental data are digitized from Ref. [81], which are fit to infared spectra based on a semi-quantum dielectric function model.

related to peaks in the one-phonon DOS.

Figure 4.6 contains the reflectance computed from the dielectric functions at 295 and 6 K shown in Figs. 4.4 and 4.5. As in the case of pure MgO, the agreement between theory and experiment is better in the region where the self-energy caused by lowest-order pertubation is large. Near the Reststrahlen frequency ω_{TO}, the self-energy is smaller, and $R(\omega)$ is more sensitive to details. Our model underestimates the broadening of the resonance, but correctly identifies the sources of broadening.

It is of interest to determine whether the disorder scattering is mainly due to the differences in mass or in the inter-atomic potential. Thus we repeat the above procedure with a model which only contains mass disorder, i.e. Fe is treated as an isotope of Mg, its shell parameters are the same as Mg^{2+} in S-I model. It turns out the most significant factor is ϵ_{∞}. For the isotope model (S-I) ϵ_{∞} is the same as pure MgO (2.94), for S-II model ϵ_{∞} increases to 3.05 for 6% Fe and 3.47 for 27%, in reasonable agreement with the results shown in Table 4.1. The LO frequency predicted from the isotope model is larger than the experimental value. The differences in the inter-atomic potentials change the relative strength of the self-energy, but in both cases the self-energy spectra carry features of the one phonon DOS of pure MgO.

In addition to phonons, electronic transitions may also influence the infrared dielectric properties of ferropericlase. Wong[82] measured the far-infrared absorption spectra of iron-doped MgO. A line at 105 cm^{-1} was observed with a peak absorption coefficient of 1.5 cm^{-1} and a width of $\simeq 9$ cm^{-1} at 20 K in a sample with 0.2% Fe. This feature is attributed to the transition $\Gamma_{5g} \rightarrow \Gamma_{3g}, \Gamma_{4g}$ of MgO: Fe^{2+} at cubic sites. If we assume the absorption coefficient is proportional to the impurity concentration, then we can estimate the corresponding ϵ_2 at 105 cm^{-1} by $\epsilon_2(\omega) = \frac{n\alpha(\omega)}{2\pi\omega}$, where n is the refractive index (for pure MgO, $n \simeq 3.2$ at 105 cm^{-1}), $\alpha(\omega)$ is the absorption
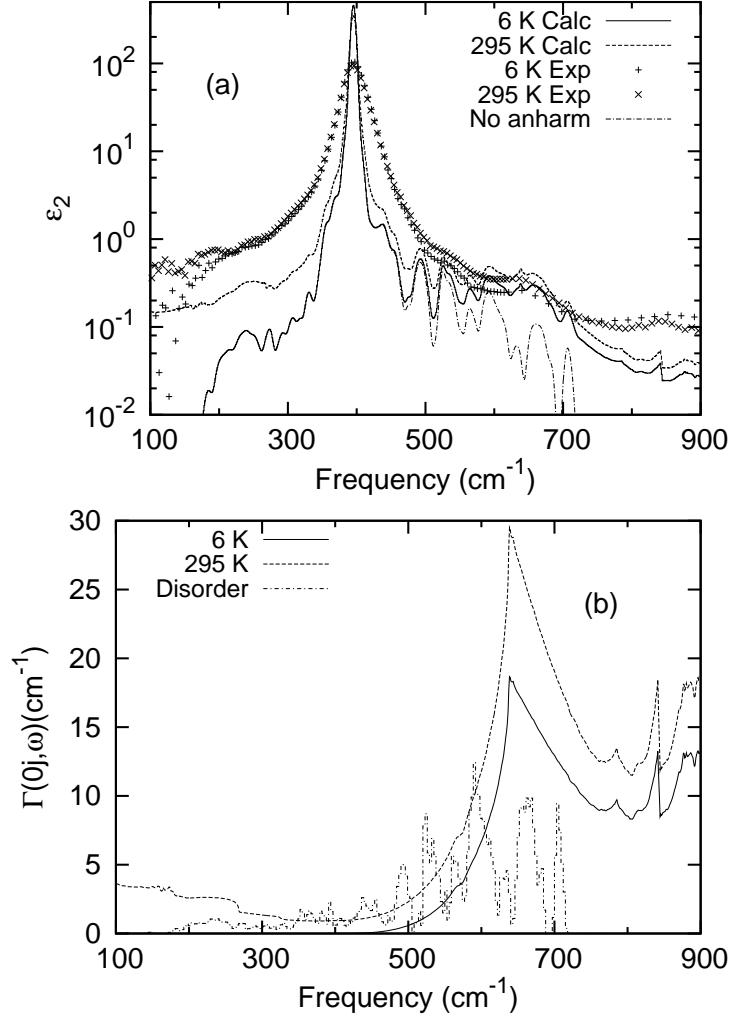
Figure 4.4: The anharmonic and disordering scattering effects in $Mg_{1-x}Fe_xO$ for the 6% Fe-doped sample. (a) Imaginary part of the dielectric function. The labels '6 K Calc' and '295 K Calc' denote the calculated curves, including both disorder scattering and anharmonic interactions at the corresponding temperature. Experimental data are the same as those in Fig. 4.1(f). The label 'No anharm' denotes the dielectric function calculated from disorder scattering only. (b) Imaginary part of self energy. The labels '6 K' and '295 K' denote the self-energies caused by anharmonic interaction at the corresponding temperature; 'disorder' denotes the self-energy due to disorder scattering, which is computed by histogram method where the bin size equals 1 cm^{-1}, then iteratively averaged 30 times. The total self-energies are the sum of these two pieces, and are used in calculating the '6 K Calc' and '295 K Calc' dielectric functions shown in (a).
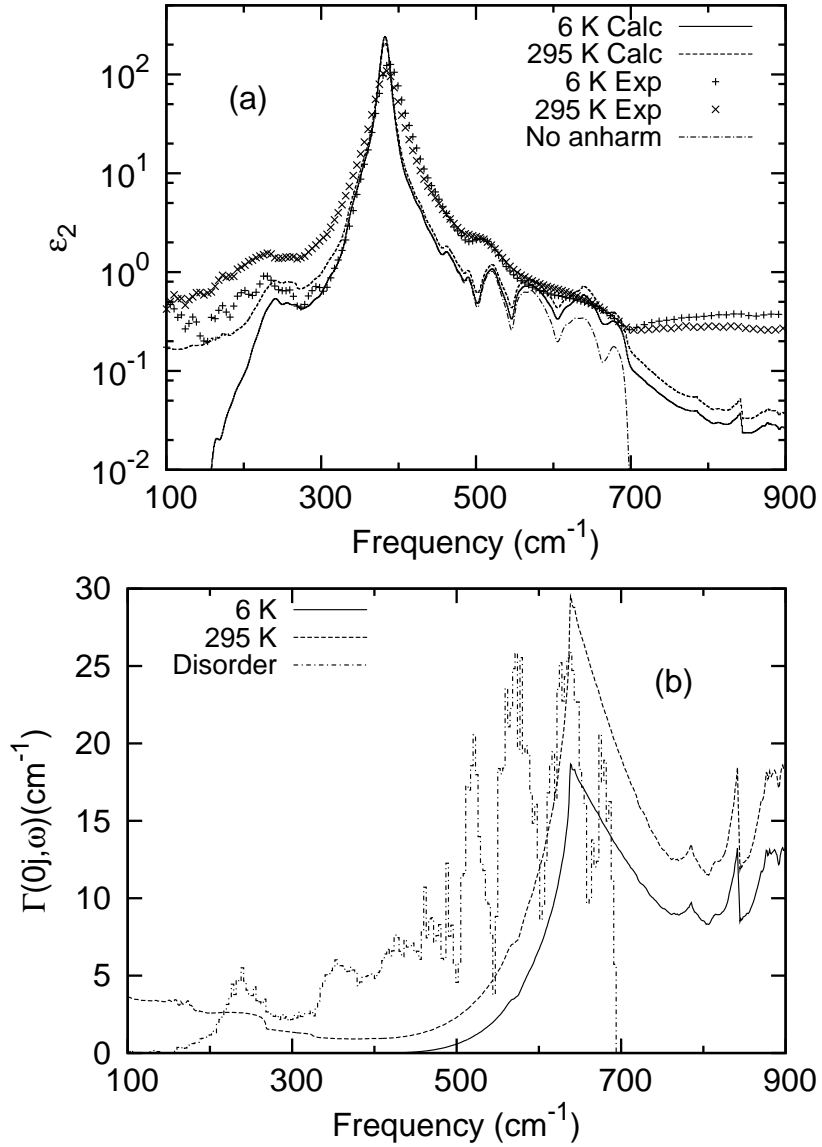
67

Figure 4.5: The anharmonic and disordering scattering effects in $Mg_{1-x}Fe_xO$ for the 27% Fe-doped sample. (a) Imaginary part of the dielectric function; (b) Imaginary part of self energy. The computation procedure is the same as for the 6% Fe doping.
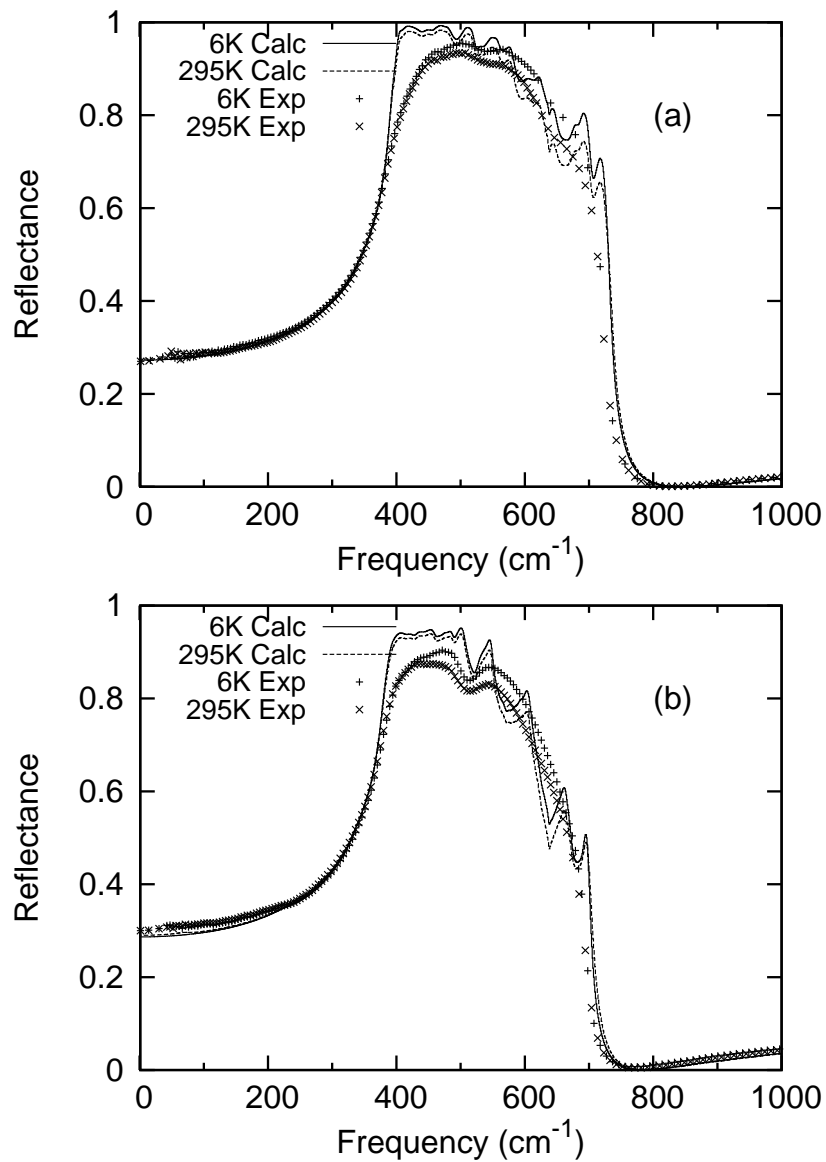
Figure 4.6: The calculated infrared reflectance, compared with the experimental data (same as in Fig. 4.1(b) and (c)) for $Mg_{1-x}Fe_xO$. (a) 6% Fe doping; (b) 27% Fe doping.

coefficient at frequency ω (in units of cm^{-1}). The value of ϵ_2 is about 0.22 for 6% Fe concentration, 0.98 for 27%. As the iron concentration x increases, the electronic transitions of Fe^{2+} should show greater influence on the far-infrared spectra of ferropericlase. In our measurement the spectra below 200 cm^{-1} are complicated due to the presence of fringes, consequently we can not confirm this tendency. Henning *et al.*[83] measured the infrared reflectance of Fe$_x$Mg$_{1-x}$O from $x=$ 0.4 to 1.0 at room temperature. The ϵ_2 curves reported in their paper do not show a monotonic rise in the far-infrared region as the iron concentration x increases from 0.4 to 1.0, while ϵ_2 is always in the range of 6-10 near 100 cm^{-1}. It is difficult to explain such large ϵ_2 with lattice vibrations alone, and the accuracy of these data has been questioned.[84] Further experiments are needed to clarify this issue.

4.5 Conclusions

The infrared reflectance spectra of magnesium oxide and ferropericlase have been measured at 295 and 6 K. It is found that ϵ_∞ increases as iron concentration increases, while the width of the TO modes remains the same in the doped materials. We construct a theoretical model which includes both disorder scattering and anharmonic phonon-phonon interactions. The model shows fairly good agreement with the experiment in the regions where the lowest-order perturbation is relatively large. Near the resonance, theory and experiment both have smaller self-energies, which makes the reflectance quite sensitive to the details. We do not know whether the disagreements with experiment in the region are caused by neglect of higher order corrections, or by inaccuracy of the underlying model. However, the model identifies the global features reasonably well, and may provide a good basis for understanding

the vibrational properties of the ferropericlase.

Bibliography

[1] N. C. Holmes, J. A. Moriarty, G. R. Gathers, and W. J. Nellis. *J. Appl. Phys.*, 66:2962, 1989.

[2] E. Menéndez-Proupin and A. K. Singh. *Phys. Rev. B*, 76:054117, 2007.

[3] A. Dewaele, P. Loubeyre, and M. Mezouar. *Phys. Rev. B*, 70:094112, 2004.

[4] P. I. Dorogokupets and A. R. Oganov. *Phys. Rev. B*, 75:024115, 2007.

[5] R. G. McQueen, S. P. Marsh, J. W. Taylor, J. M. Fritz, and W. J. Carter. In R. Kinslow, editor, *High Velocity Impact Phenomena*, chapter 7. Academic press, New York, 1970.

[6] O. L. Anderson. *Equations of State of Solids for Geophysics and Ceramic Science.* Oxford Univ. Press, 1995.

[7] F. Birch. *Phys. Rev.*, 71:809, 1947.

[8] P. Vinet, J. R. Smith, J. Ferrante, and J. H. Rose. *Phys. Rev. B*, 35:1945, 1987.

[9] R. M. Martin. *Electronic Structure: Basic Theory and Practical Methods.* Cambridge Univ. Press, 2004.

[10] J. Kohanoff. *Electronic Structure Calculations for Solids and Molecules.* Cambridge Univ. Press, 2006.

[11] P. Hohenberg and W. Kohn. *Phys. Rev.*, 136:864, 1964.

[12] J. P. Perdew and A. Zunger. *Phys. Rev. B*, 23:5048, 1981.

[13] J. P. Perdew, K. Burke, and M. Ernzerhof. *Phys. Rev. Lett.*, 77:3865, 1996.

[14] D. R. Hamann, M. Schluter, and C. Chiang. *Phys. Rev. Lett.*, 43:1494, 1979.

[15] W. E. Pickett. *Comp. Phys. Rep.*, 9:115, 1989.

[16] D. Vanderbilt. *Phys. Rev. B*, 41:7892, 1990.

[17] X. Gonze, P. Kackell, and M. Scheffler. *Phys. Rev. B*, 41:12264, 1990.

[18] J. A. Morgan. *High Temp. High Pressures*, 6:195, 1974.

[19] J. C. Jamieson, J. N. Fritz, and M. H. Manghnani. In S. Akimoto and M. H. Manghnani, editors, *High-Pressure Research in Geophysics*. Cent. for Acad. Publ., Tokyo, 1982.

[20] H. K. Mao, Y. Wu, L. C. Chen, and J. F. Shu. *J. Geophys. Res.*, 95:21737, 1990.

[21] F. D. Stacey and P. M. Davis. *Phys. Earth Planet. Inter.*, 142:137, 2004.

[22] A. K. Singh. *Phys. Earth Planet. Inter.*, 164:75, 2007.

[23] Y. W. Fei, A. Ricolleau, M. Frank, K. Mibe, G. Shen, and V. Prakapenka. *Proc. Natl. Acad. Sci. USA*, 104:9182, 2007.

[24] C. S. Zha, K. Mibe, W. A. Bassett, O. Tschauner, H. K. Mao, and R. J. Hemley. *J. Appl. Phys.*, 103:054908, 2008.

[25] S. K. Xiang, L. C. Cai, Y. Bi, F. Q. Jing, and S. J. Wang. *Phys. Rev. B*, 72: 184102, 2005.

[26] There are two LDA ultrasoft Rappe-Rabe-Kaxiras-Joannopoulos pseudopotentials on the PWSCF (www.pwscf.org) website. 'Pt.pz-rrkjus.UPF' is the one without nonlinear core correction 'Pt.pz-nd-rrkjus.UPF' includes this correstion. Both have a cutoff radius of 2.6 a.u., both yield static EOS stiffer than that of Holmes *et al*. The results reported in PRB (76) 054117 (2007) are very close to our calculations using 'Pt.pz-nd-rrkjus.UPF'.

[27] Y. W. Fei, J. Li, K. Hirose, W. Minarik, J. V. Orman, C. Sanloup, W. V. Westrenen, T. Komabayashi, and K. Funakoshi. *Phys. Earth Planet. Inter.*, 143-144:515, 2004.

[28] D. H. Dutton, B. N. Brockhouse, and A. P. Miller. *Can. J. Phys.*, 50:2915, 1972.

[29] P. Blaha, K. Schwarz, G. K. H. Madsen, D. Kvasnicka, and J. Luitz. In K. Schwarz, editor, *WIEN2k: An Augmented Plane Wave and Local Orbitals Program for Calculating Crystal Properties*. Vienna University of Technology, Vienna, Austria, 2001.

[30] J. P. Perdew, K. Burke, and M. Ernzerhof. *Phys. Rev. Lett.*, 77:3865, 1996.

[31] Z. Wu and R. E. Cohen. *Phys. Rev. B*, 73:235116, 2006.

[32] H. J. Monkhorst and J. D. Pack. *Phys. Rev. B*, 13:5188, 1976.

[33] P. E. Blőchl, O. Jepsen, and O. K. Andersen. *Phys. Rev. B*, 49:16223, 1994.

[34] S. G. Louie, S. Froyen, and M. L. Cohen. *Phys. Rev. B*, 26:1738, 1982.

[35] M. Methfessel and A. T. Paxton. *Phys. Rev. B*, 40:3616, 1989.

[36] N. D. Mermin. *Phys. Rev.*, 137:A1441, 1965.

[37] S. Baroni, P. Giannozzi, and A. Testa. *Phys. Rev. Lett.*, 58:1861, 1987.

[38] S. Baroni, A. DalCorso, S. de Gironcoli, P. Giannozzi, C. Cavazzoni, G. Ballabio, S. Scandolo, G. Chiarotti, P. Focher, A. Pasquarello, K. Laasonen, A. Trave, R. Car, N. Marzari and A. Kokalj, http://www.pwscf.org/.

[39] R. E. Cohen, O. Gülseren, and R. J. Hemley. *Am. Mineral.*, 85:338, 2000.

[40] T. Tsuchiya and K. Kawamura. *Phys. Rev. B*, 66:094115, 2002.

[41] T. Tsuchiya. *J. Geophys. Res.*, 108(B10):2462, 2003.

[42] Y. Wang, R. Ahuja, and B. Johansson. *J. Appl. Phys.*, 92:6616, 2002.

[43] C. Bercegeay and S. Bernard. *Phys. Rev. B*, 72:214101, 2005.

[44] A. D. Chijioke, W. J. Nellis, and I. F. Silvera. *J. Appl. Phys.*, 98:073526, 2005.

[45] A. Dewaele, private communication.

[46] P. I. Dorogokupets and A. Dewaele. *High Pressure Res.*, 27:431, 2007.

[47] A. DalCorso and A. M. Conte. *Phys. Rev. B*, 71:115106, 2005.

[48] this TM pseudopotential is constructed from $5d^96s^{0.95}6p^{0.05}$ atomic configuration, the cutoff radius of $6s$ is 2.6 a.u., which is probably too large. The HGH pseudopotential is constructed from $5s^25p^65d^{10}$ and does not have this problem.

[49] A. Kavner and R. Jeanloz. *J. Appl. Phys.*, 83:7553, 1998.

[50] R. A. Cowley. *Rep. Progr. Phys.*, 31, part 1:123, 1968.

[51] P. B. Allen and J. C. K. Hui. *Z. Physik B*, 37:33, 1980.

[52] J. Xie, S. de Gironcoli, S. Baroni, and M. Scheffler. *Phys. Rev. B*, 59:965, 1999.

[53] S. Narasimhan and S. de Gironcoli. *Phys. Rev. B*, 65:064302, 2002.

[54] R. K. Kirby. *Inter. J. of Thermophys.*, 12:679, 1991.

[55] J. W. Arblaster. *Platinum Metals Rev.*, 38(3):119, 1994.

[56] S. M. Collard and R. B. McLellan. *Acta Metall. Mater.*, 40:699, 1992.

[57] J. D. Jackson. *Classical Electrodynamics*. John Wiley & Sons, Inc., 1975.

[58] A. A. Maradudin and A. E. Fein. *Phys. Rev.*, 123:2589, 1962.

[59] R. J. Elliott, J. A. Krumhansl, and P. L. Leath. *Rev. Mod. Phys.*, 46:465, 1974.

[60] G. K. Horton and A. A. Maradudin, editors. *Dynamical Properties of Solids*, volume 2, chapter 5. North-Holland Publishing Company, 1975.

[61] B. G. Dick and A. W. Overhauser. *Phys. Rev.*, 112:90, 1958.

[62] G. Venkataraman, L. A. Feldkamp, and V. C. Sahni. *Dynamics of Perfect Crystals*. MIT Univ. Press, 1975.

[63] B. Donovan and J. F. Angress. *Lattice Vibrations*. Chapman & Hall LTD, 1971.

[64] T. Yagi and N. Funamori. *Phil. Trans.*, 354:1711, 1996.

[65] D. M. Roessler and W. C. Walker. *Phys. Rev.*, 159:733, 1967.

[66] A. F. Goncharov, V. V. Struzhkin, and S. D. Jacobsen. *Science*, 312:1205, 2006.

[67] H. Keppler, I. Kantor, and L. S. Dubrovinsky. *Am. Mineral.*, 92:433, 2007.

[68] J. R. Jasperse, A. Kahan, and J. N. Plendl. *Phys. Rev.*, 146:526, 1966.

[69] S. D. Jacobsen, H. J. Reichmann, H. A. Spetzler, S. J. Mackwell, J. R. Smyth, R. J. Angel, and C. A. McCammon. *J. Geophy. Res.*, 107, No. B2:ECV 4, 2002.

[70] C. C. Homes, M. Reedyk, D. A. Crandles, and T. Timusk. *Appl. Opt.*, 32:2972, 1993.

[71] J. Fabian and P. B. Allen. *Phys. Rev. Lett.*, 77:3839, 1996.

[72] J. D. Gale. *JCS Faraday Trans.*, 93:629, 1997.

[73] A. M. Stoneham and M. J. L. Sangster. *Phil. Mag. B*, 52:717, 1985.

[74] M. J. L. Sangster. *J. Phys. Chem. Solids*, 34:355, 1973.

[75] M. J. L. Sangster, G. Peckham, and D. H. Saunderson. *J. Phys. C: Solid State Phys.*, 3:1026, 1970.

[76] G. Kugel, C. Carabatos, B. Hennion, B. Prevot, A. Revcolevschi, and D. Tocchetti. *Phys. Rev. B*, 16:378, 1977.

[77] M. J. L. Sangster and A. M. Stoneham. *Phil. Mag. B*, 43:597, 1981.

[78] E. R. Cowley. *J. Phys. C: Solid State Phys.*, 5:1345, 1972.

[79] L. Bohlin and T. Högberg. *J. Phys. Chem. Solids*, 29:1805, 1968.

[80] A. D. Bruce. *J. Phys. C: Solid State Phys.*, 6:174, 1973.

[81] D. D. S. Meneses, J. Brun, P. Echegut, and P. Simon. *Appl. Spectro.*, 58:969, 2004.

[82] J. Y. Wong. *Phys. Rev.*, 168:337, 1968.

[83] T. Henning, B. Begemann, H. Mutschke, and J. Dorschner. *Astron. Astrophys. Suppl. Ser.*, 112:143, 1995.

[84] A. M. Hofmeister, E. Keppel, and A. K. Speck. *Mon. Not. R. Astron. Soc.*, 345:16, 2003.